Mineralogical and geochemical study of serpentinized peridotites from the North-Western Pyrenees: New insights on serpentinization along magma-poor continental passive margins

C. Tichadou, M. Godard, M. Muñoz, P. Labaume, A. Vauchez, E.C. C Gaucher, S. Calassou

Mineralogical and geochemical study of serpentinized peridotites from the North-Western Pyrenees: New insights on serpentinization along magma-poor continental passive margins

C. Tichadou [a], M. Godard [a,*], M. Muñoz [a], P. Labaume [a], A. Vauchez [a], E.C. Gaucher [b], S. Calassou [b]

[a] Géosciences Montpellier, CNRS, Université de Montpellier, Place Eugène Bataillon, 34095 Montpellier cedex, 5, France
[b] TOTAL, CSTJF, Avenue Larribau, 64018 Pau Cedex, France

ARTICLE INFO

Keywords:
Passive margin
Pyrenees
Serpentinization
Iron distribution
Hydrogen

ABSTRACT

The peridotite massifs from the North-Western Pyrenean belt are fragments of a short-lived mid-Cretaceous hyper-extended rift inverted by the Pyrenean orogeny. We studied the petrology, mineralogy and geochemistry of 32 hydrothermally altered peridotites from the Montaut, Turon and Urdach massifs. This study aims to bring new constraints on the nature of serpentinization processes from domains having experienced various degrees of crustal hyper-extension and mantle exhumation in a context analogous to non-volcanic ocean-continent transitions.

The three massifs studied are mainly composed of spinel-lherzolites and sample the same sub-continental mantle lithosphere as Eastern Pyrenean refertilized-peridotite massifs. They display contrasted degrees of hydrothermal alteration and serpentinization during cooling (e.g., serpentine contents ranging from 1 to 100 wt%) as well as variable reaction paths. The Montaut massif, located below an extremely thinned Paleozoic upper crust, records cooling from high temperature hydrothermalism with incipient serpentinization affecting mostly pyroxenes (serpentine, tremolite, talc, clinochlore assemblage; ~350–450 °C) to the formation of lizardite-chrysotile and magnetite after olivine (~200 °C–350 °C). The Turon peridotites, which remained below the detached Mesozoic pre-rift cover after complete removal of the crust, are little serpentinized and have no magnetite, suggesting serpentinization during the latest stages of cooling (< 200 °C). The Urdach massif comprises magnetite-bearing ophicalcites as well as magnetite-poor serpentinites formed concurrently when mantle was exhumed to the sub-seafloor at the margin toe (down to ~200 °C). Each massif shows selective enrichments in fluid mobile elements, in particular, Cs, Sb and Li, indicative of hydrothermal interactions with fluids deriving from neighboring sediments and continental crust, likely mixed with seawater-derived fluids for the Urdach peridotites. Our results show that the formation of magnetite in the studied samples is not tied solely to temperature, and point to a role of fluid composition in the development of the different serpentinization pathways observed from one massif to the other, and within a same massif in the case of Urdach.

The development of complex sequences of temperature-, and composition-controlled reaction paths distinguish serpentinization in the Western Pyrenees peridotites from that commonly observed in the oceanic sub-seafloor. It results in variable redistribution of iron between magnetite and serpentine minerals, with the predominance of Fe-rich lizardite in magnetite-poor serpentinized peridotites. It likely controls local redox conditions and H_2 production; suggesting that the impacts of serpentinization on the production of dihydrogen will vary from passive margins to oceanic sub-seafloor.

1. Introduction

Serpentinization results from the hydrothermal interaction, at temperatures below ~450 °C, between aqueous fluids and the Mg-Fe-rich minerals of the lithospheric mantle (olivine and pyroxenes) (e.g., Evans et al., 2013; Mével, 2003). It involves a suite of hydration and

https://doi.org/10.1016/j.lithos.2021.106521

redox reactions (see examples of balanced reactions in Marcaillou et al., 2011) that can be written as:

$$(Mg, Fe) - Olivine + (Mg, Fe) - Pyroxene + H_2O \rightarrow (Mg, Fe) - Serpentine + Magnetite + H_2 \quad (1)$$

The formation of hydrous mineral serpentine is commonly associated to that of additional hydrous phases (brucite, talc), carbonates, oxides and sulfides depending on temperature (e.g., Bach et al., 2004; Evans, 2008; Klein et al., 2013b; Malvoisin et al., 2012; Mével, 2003; Seyfried et al., 2007), the respective amounts of Mg-Fe-rich mantle minerals (e.g., Frost and Beard, 2007; Klein et al., 2009) and the composition(s) of serpentinizing fluid(s) (e.g., Frost, 1985; Peuble et al., 2015; Schwarzenbach et al., 2013). This suite of reactions has important implications for plate tectonics and global (bio-)geochemical cycles (e.g., Deschamps et al., 2013; Escartín et al., 2003; Klein et al., 2015). They could also represent an alternative and natural source of carbon-free energy via dihydrogen production and CO_2 mineralization reactions (carbonation) (e.g., Gaucher, 2020; Kelemen et al., 2011).

Serpentinization is common where mantle is tectonically exposed along the divergent limits of tectonic plates and continents such as non-volcanic oceanic spreading centers and passive margins (e.g., Evans et al., 2013; Guillot et al., 2015; Mével, 2003; Pérez-Gussinyé and Reston, 2001). It modifies the chemical and physical properties of the lithospheric mantle (e.g., Bach et al., 2004; Evans et al., 2013; Mével, 2003; Paulick et al., 2006) and by reducing the strength of peridotites to that of serpentines, it favors the development of large detachment faults (e.g., Escartín et al., 2003). These tectonic processes are considered as a major mechanism for the exhumation of deep mantle domains at ocean-continent transitions (OCT, e.g., Guillot et al., 2015; Manatschal, 2004; Pérez-Gussinyé and Reston, 2001). Extreme thinning of the continental crust and faulting allow fluids to infiltrate the lithospheric mantle down to depths of 10–15 km (e.g., Boillot and Beslier, 1992; Manatschal, 2004). Yet, in spite of its importance for understanding continental break-up and incipient oceanization, serpentinization at passive margins remains poorly constrained. The main reason is the geological complexity over which hydrothermal processes can take place in these domains, from the cold and thick continental lithosphere to deep oceanic subseafloor.

Most of our understanding of the mineralogical and (bio-)geochemical processes associated to serpentinization at passive margins is based on the study of serpentinized peridotites drilled during the Ocean Drilling Program (1985–2003) along the conjugate Iberian-Newfoundland Margins. These studies have revealed that serpentinization in this most oceanward domain of a magma-poor passive margin was taking place at low temperatures (<200 °C) in contrast to mid-ocean ridge serpentinizing environments (e.g., Albers et al., 2021; Klein et al., 2015; Schwarzenbach et al., 2013). This difference in serpentinization conditions between these oceanic domains raises the question of the mineralogical and geochemical impact(s) of further changes in hydrothermal conditions closer to the continent. Mantle peridotites from fossil OCTs in Alpine orogenic belts expose both the continental and oceanic end-members of fossil passive margins (e.g., Tasna (Manatschal et al., 2006); Lower Platta (Muntener et al., 2009); and Totalp (Van Acken et al., 2008) in the Alps) thus representing a unique opportunity to document these processes (e.g., Manatschal, 2004).

This study focusses on the North Pyrenean orogenic belt that preserves relics of subcontinental mantle exhumed in a distal margin setting during the mid-Cretaceous rifting that preceded the Pyrenean convergence (e.g., Clerc et al., 2012; Lagabrielle et al., 2010; Lagabrielle and Bodinier, 2008; Teixell et al., 2018). We present the result of a petrological, mineralogical and geochemical study of variously serpentinized peridotites from three peridotite massifs of the Chaînons Béarnais (Western Pyrenees) (Fig. 1). The Urdach-Les Pernes (thereafter referred to as Urdach) has been interpreted as representative of the most basinward (distal) domain of the Pyrenean rift, where the mantle was exhumed to the sea-floor (e.g., Lagabrielle et al., 2019a; Lagabrielle et al., 2019b). The Turon de la Técouère (thereafter referred to as Turon) and Montaut massifs have more proximal positions in this system although both belong to hyper-extended domains (Lagabrielle et al., 2010). The aim of the study was: (1) to determine the nature of the mantle protolith, (2) to identify the sequences of alteration, from rifting to convergence, and (3) the nature of the fluids involved in these processes. These results were used to discuss the conditions and reaction paths for serpentinization along magma-poor passive margins.

2. Geological setting and sampling strategy

2.1. Geology of the Pyrenees

The Pyrenean orogen is a 400 km east-west trending continental fold and thrust mountain belt (Fig. 1a) resulting from the convergence between the Iberia and Eurasia plates during the Late Cretaceous-Cenozoic (see Teixell et al., 2018, and references therein). It followed a major episode of rifting associated with the plate motion of Iberia with respect to Eurasia during the mid-Cretaceous opening of the North Atlantic and the Bay of Biscay oceanic domains. Continental thinning and mantle exhumation occurred along the margins of the Iberia and Eurasia continental plates. Hyper-extension of the distal margins locally resulted in the complete removal of the continental crust in the rift axis, with the pre-rift Mesozoic cover detached along the Upper Triassic directly resting above the exhumed mantle, or even with local outcrops of mantle rocks at the sea-floor (e.g., Clerc and Lagabrielle, 2014; Lagabrielle et al., 2010). The high thermal gradient resulting from mantle unroofing induced a high temperature (HT) and low pressure (LP) metamorphism of the Mesozoic sediments, with a decreasing intensity from the Eastern (500–600 °C) to the Western Pyrenees (around 300–350 °C, with local maxima close to 500 °C) (e.g., Clerc et al., 2015). As the Iberia plate started converging toward the European plate (Late Santonian), the rifted domains were inverted, and peridotite bodies were pinched into what became the North Pyrenean Zone (NPZ), an east-west trending domain limited to the south by the belt Axial Zone and to the north by the North Pyrenean Frontal Thrust (NPFT; e.g., Teixell et al., 2018).

Forty peridotite massifs, up to a few kilometers across, outcrop along the NPZ, embedded into Mesozoic sediments and often associated with bodies of Paleozoic crust (e.g., Fabriès et al., 1998; Fabriès et al., 1991; Fig. 1a). The peridotites comprise dominantly spinel lherzolites associated to subordinate harzburgites, and abundant pyroxenites (see review in Bodinier and Godard, 2013). The Eastern Pyrenees (EP) peridotites are distinguished by the occurrence of high temperature amphibole-pyroxenite dykes crosscutting metasomatized harzburgitic protoliths, in association to Cretaceous alkali magmatism, previous and/or contemporaneous to crustal thinning and mantle exhumation (e.g., Bodinier et al., 1988; Bodinier et al., 1990; Fabriès et al., 1991). The peridotites exposed in the Central and Western Pyrenees (Fig. 1a, thereafter referred to as Western Pyrenees (WP) peridotites) are characterized by the prevalence of clinopyroxene-rich foliated spinel peridotites and the greater development of low temperature-high stress textures (e.g., mylonites, Fabriès et al., 1991; Vissers et al., 1997). They comprise variously clinopyroxene-rich lherzolites often associated with

spinel websterites and rare harzburgites. Amphibole is occasionally observed associated to subsolidus re-equilibration textures, such as the fine disseminated Ti-pargasite and plagioclase forming after spinel (e.g., Turon) or hydrothermal actinolite replacing pyroxenes (e.g., Urdach). Fabriès et al. (1998) demonstrated that these characteristics reveal contrasting petrogenetic pathways for the EP and WP peridotites. First, the WP peridotites record a stage of decompression (1050–950 °C; 50-60 km to ~25 km) similar to the single decompression cooling stage associated to lithospheric thinning recorded by the EP peridotites. Then, they record a second stage of uplift and cooling (down to 600 °C) and

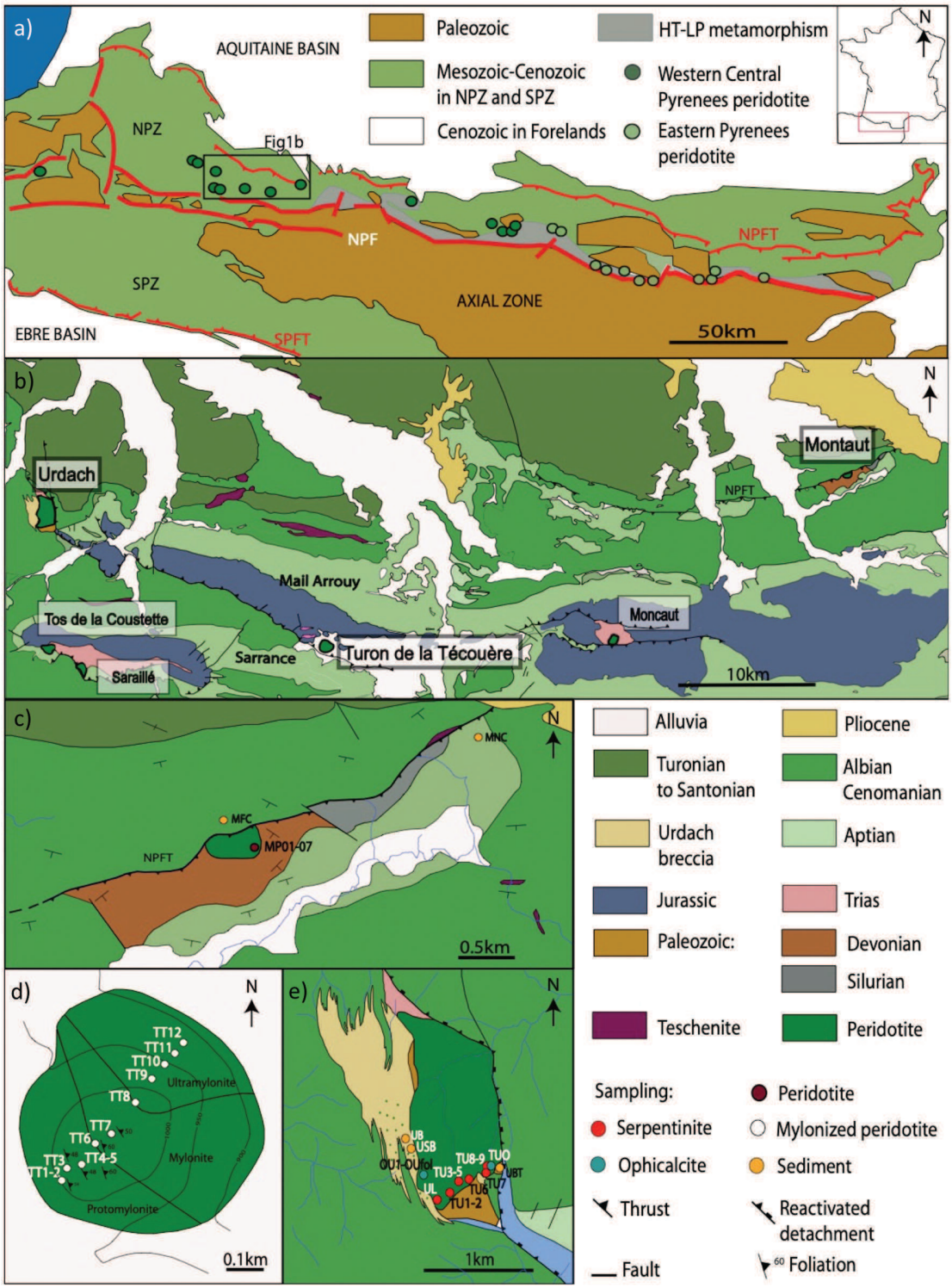

Fig. 1. a) Geological map of the Pyrenees with location of the main peridotite massifs (modified after Clerc et al., 2012). b) Geological map of the northern part of the Chaînons Béarnais with location of the peridotite massifs after BRGM 1:50000 geological maps. Sampling locations in the c) Montaut massif, d) Turon massif (after Vissers et al., 1997), e) Urdach massif (after Lagabrielle et al., 2019b).

equilibrate at depths significantly shallower compared to the EP peridotites. This second stage of mantle exhumation recorded by the WP peridotites was likely coeval to the mid-Cretaceous rifting. The fast cooling, high-stress deformation, and tectonic denudation recorded by WP peridotites represent a sequence of processes analogous to those affecting peridotites exhumed at OCTs (Manatschal et al., 2006).

2.2. Sampling the peridotites of the Chaînons Béarnais (Western Pyrenees)

We studied three WP massifs, Turon, Montaut and Urdach (Fig. 1b), all part of the Chaînons Béarnais, a 50 km-long segment of the western NPZ (Fig. 1b) constituted by a system of *E*-W trending Jurassic to Aptian carbonate ridges (Labaume and Teixell, 2020). The peridotite bodies occur at, or close to, the base of the Mesozoic succession and structural restauration links the studied massifs to the evolution of the European margin of the mid-Cretaceous rift system (e.g., Lagabrielle et al., 2019a; Lagabrielle et al., 2019b). Most of the available information on the petrology and geochemistry of these peridotite bodies results from the studies of Fabriès et al. (1991, 1998).

i) *Montaut massif*

The Montaut massif is a 0.45 km wide peridotite body located at the hanging wall of the NPFT and overlain by about 200 m of Devonian schists themselves covered by Aptian limestone followed by Albian flysch (Fig. 1b-c). The massif is thrust northward by the NPFT above an overturned series of Upper Cretaceous flysch (Labaume and Teixell, 2020) and has been little investigated before this study. It comprises dominantly highly serpentinized lherzolites (Fabriès et al., 1991; Fabriès et al., 1998). Two peridotite outcrops were selected for sampling: (1) an ancient quarry of massive and highly serpentinized peridotites (6 samples) cross-cut by pyroxenites (1 sample; Fig. 1c); and (2) the newly exposed contact with the NPFT along a recent road (7 samples). Close to the NPFT, a lenticular layer composed of a sheared talc-bearing serpentinized lherzolite was observed (see supplementary Fig. A1); it is a common feature in the NPZ peridotite bodies, often associated to chlorite (Lagabrielle et al., 2019a). However, preliminary investigations showed that the geochemistry of the NPFT peridotites has been significantly modified by pedogenetic alteration so we focused our study on the quarry samples. Two sediments were collected: one sample of Cenomanian flysch at the footwall of the NPFT, and one sample of Aptian limestone located at the east of the peridotite body (Fig. 1c).

ii) *Turon massif*

The Turon peridotite massif, on the Bénou plateau, is a hill of about 700 m diameter bounded by Quaternary glacial deposits (Fig. 1b, d). It is embedded in the Upper Triassic complex (Keuper facies, carbonates and ophite) at the base of the Mail Arrouy thrust unit (Labaume and Teixell, 2020). The Turon peridotites are little to moderately serpentinized lherzolites mylonitized in the stability field of spinel or plagioclase. Their microstructure gradually switches from SW to NE, from protomylonites to mylonites then ultramylonites; while spinel is progressively replaced by plagioclase, indicating that mylonitization occurred during exhumation (Vissers et al., 1997). Protomylonites and mylonites display a moderately to steeply N*E*-dipping foliation and a gently SE-plunging to subhorizontal lineation (Vissers et al., 1997) suggesting transtensional exhumation. 5 protomylonites (i.e., <50% of fine-grained matrix), 2 mylonites (i.e., fine-grained matrix between 50 and 90%) and 5 ultramylonites (i.e., >90% of fine-grained matrix) were collected along a S—N transect (Fig. 1d). Two samples of sedimentary rocks were collected: one from a lens of Triassic marl located 300 m north of the Turon massif, and one of Upper Aptian limestone from the quarry located in the footwall of the Mail Arrouy thrust, 500 m south of the massif.

iii) *Urdach massif*

The Urdach massif is a 1.5 km peridotite body located at the western termination of the Mail Arrouy thrust unit (Fig. 1b). Lagabrielle et al. (2019b) proposed that the massif is deformed by a west-vergent anticline. To the west, the peridotite massif is stratigraphically overlain by a sedimentary breccia comprising abundant talc-bearing and serpentinized peridotites, Paleozoic continental crustal rocks and subordinate Mesozoic sediments, and it shows lateral transitions to the upper Albian *syn*-rift flysch. Hectometer-sized lenses of Paleozoic continental crust are locally intercalated between the peridotite and the breccia (Lagabrielle et al., 2019b; Lagabrielle et al., 2010; Fig. 1e). On its eastern side, the massif is separated from the Mail Arrouy Mesozoic series by a fault system corresponding to the merging of two major low-angle extensional shear zones now inverted by the Pyrenean orogeny: (1) the crust-mantle detachment, a deep structure located between the subcontinental mantle and Paleozoic continental crust, and (2) the cover décollement, a shallow structure, located in the Upper Triassic Keuper facies at the base of the pre-rift Mesozoic sediments (Lagabrielle et al., 2019a, 2019b; Fig. 1e).

The Urdach massif comprises: (1) serpentinites in the central part of the massif, and (2) variously carbonated and serpentinized peridotites (ophicalcites) in two quarries at the SW and SE limits of the massif. The presence of ophicalcites, sedimentary breccias with peridotites and Paleozoic clasts and of the breccia-flysch lateral transitions was interpreted as evidence of seafloor exposure occurring at the end of Albian (e.g., Clerc et al., 2013; Lagabrielle et al., 2010). We sampled 9 serpentinites and 4 ophicalcites along an E-W transect in the southern part of the massif (Fig. 1e). Two brecciated peridotites from the Urdach breccia, and one sample of Cretaceous flysch were also collected to the south-east of the massif (Fig. 1e).

3. Methods

3.1. Analytical methods

The structure, lithology and mineralogy of the 32 WP samples were determined from field and hand sample observations, optical microscopy, X-Ray Diffraction (XRD) and Raman spectroscopy. Mineral compositions were analyzed in-situ by Electron Probe Micro-Analyzer (EPMA) and Laser Ablation Inductively Coupled Plasma Mass Spectrometry (LA-ICP-MS). The bulk rock geochemistry of the samples was determined using X-Ray Fluorescence (XRF) and Inductively Coupled Plasma Mass Spectrometry (ICP-MS). Sample preparation, analytical and data processing protocols are reported in Supplementary Material A1, and summarized thereafter.

XRD analyses were performed on powders with a Malvern Panalytical X-Pert PRO diffractometer (RRXG facility, Charles Gerhardt Institute, University of Montpellier, France), using a large X-ray beam emitted by a Cu- K-alpha beam with 45 kV accelerating voltage and 30 mA current. XRD data were processed using PROFEX (Doebelin and Kleeberg, 2015). Identified minerals and modal estimates are reported in Supplementary Material Table A2.

Raman spectroscopy was performed using a Renishaw Invia spectrometer (Charles Coulomb laboratory, Montpellier University, France)

operating with a wavelength of 532 nm and a power of 15 mW, coupled to an open microscope equipped with 50× objective or 100× objective lens, which give a spatial resolution of approximately 1–2 μm. The spectral region investigated was 100 to 3800 cm^{-1}. The Raman spectrometer was calibrated using the Si peak at 520 cm^{-1} prior to analysis. Spectral data were identified by comparison to the RRUFF spectral database (Lafuente et al., 2015).

EPMA analyses were performed with a CAMECA SX100 equipped with five wavelength-dispersive X-ray spectrometers (Géosciences Montpellier, Montpellier University, France) using a 20 kV accelerating potential and 10 mA beam current. Point analyses were realized with 30 s counting times and elementary maps (Si, Al, Mg, Fe, Ni, Cr, Ca) with a dwell time of 50 ms and a step of 3 μm. Detection limits are reported in Supplementary Material Table A3.

Bulk major element compositions were measured by XRF at Geoscience Laboratories (Ontario Geological Survey; Canada). The samples were run for Loss On Ignition (LOI), then the ignited samples were fused with a borate flux to produce the glass beads for analyses.

Bulk trace element concentrations (Li, Sc, Ti, V, Mn, Co, Ni, Cu, Zn, Ga, As, Rb, Sr, Y, Zr, Nb, Sn, Sb, Cs, Ba, Hf, Ta, Pb, Th, U and Rare Earth Elements (REE: La, Ce, Pr, Nd, Sm, Eu, Gd, Tb, Dy, Ho, Er, Tm, Yb, Lu) were measured on samples prepared in the Géosciences Montpellier clean lab facility (Montpellier University, France), using an Agilent 7700× quadrupole ICP-MS (AETE-ISO, OSU OREME, France). Procedural blanks and the values obtained for certified reference materials are reported in Supplementary Material Table A4.

In-situ trace element concentrations (Li, Sc, Ti, V, Cr, Mn, Co, Ni, Cu, Zn, Rb, Sr, Y, Zr, Nb, Sb, Ba, REE, Hf, Ta, Pb, Th and U) were determined in olivine, orthopyroxene, clinopyroxene, amphibole and serpentine by LA-ICP-MS, using a Element2 XR ICP-MS coupled to a Geolas automated platform with a 193 nm Excimer G2 (AETE-ISO, OSU OREME, France) and an Element XR ICP-MS coupled to a 193 nm Resonetics M50 Excimer Ar/F (LMV, University of Clermont-Auvergne, France). Values obtained for certified reference materials are reported in Supplementary Material Table A5.

3.2. Geothermobarometry

Pressure was calculated using the FACE geobarometer. It is based on the analysis of clinopyroxene-orthopyroxene-plagioclase-olivine assemblages in mantle peridotite (Fumagalli et al., 2017), only observed in the fine-grained matrix of the Turon peridotites.

Temperatures were determined with 3 thermometers giving decreasing closure temperatures: the T_{REE} thermometer (Liang et al., 2013), and the $T_{Ca\text{-}in\text{-}Opx}$ and $T_{2\text{-}Px}$ thermometers (Brey and Köhler, 1990; Wells, 1977). The T_{REE} thermometer is based on the distribution of REE between orthopyroxene (Opx) and clinopyroxene (Cpx) and, due to slow diffusion rates of trivalent cations relative to divalent cations in pyroxenes, it gives temperature estimates close to crystallization temperatures (Liang et al., 2013). The $T_{Ca\text{-}in\text{-}Opx}$ thermometer (TCa-in-Opx; Brey and Köhler, 1990) is calculated using the Opx Ca composition. The $T_{2\text{-}Px}$ thermometer is based on the exchange of several elements including Ca, Na, Mg and Fe between Cpx and Opx (Brey and Köhler, 1990; Wells, 1977). The diffusion of Ca in Cpx is faster than in Opx and it results that the $T_{Ca\text{-}in\text{-}Opx}$ thermometer gives higher equilibrium temperatures than the $T_{2\text{-}Px}$ thermometer.

These thermometers rely on the control of temperature and pressure on the partitioning of chemical elements between Opx and Cpx (T_{REE}, $T_{Ca\text{-}in\text{-}Opx}$) or within a single Opx ($T_{2\text{-}Px}$). We considered only samples in which we could identify mineral pairs in equilibrium. None were found in the highly altered Montaut and Urdach peridotites. Also, identifying minerals large enough to be analyzed was challenging in the Turon mylonites and ultramylonites, thus limiting the number of samples in which temperatures could be calculated.

4. Results

4.1. Petrology and mineralogy

XRD and EPMA results are reported in Supplementary Material Table A2 and A3 and summarized in Table 1.

i) Montaut massif.

The Montaut samples are coarse-grained spinel lherzolites, except sample MP03 that is crosscut by a pyroxenite vein (Fig. 2a). These samples are highly altered, showing rare relics of olivine, orthopyroxene and clinopyroxene. The serpentine content ranges between 50 and 70 wt %. Mesh serpentine, composed of a mix of lizardite and chrysotile, is observed in all samples, in association with magnetite grains aligned along mesh veins. Bastite textures are observed as a replacement, or at the rims of pyroxenes and amphibole. Amphibole (tremolite variety, 1–27 wt%) is present in all samples, along the rims of clinopyroxene (Cpx). Talc (3–15 wt%) is forming at the expanse of pyroxenes. Clinochlore (3–26 wt%) is also identified in most samples, and spinel is generally altered to ferrichromite at the rim.

Table 1
Serpentine content and characteristics in the three massifs.

	Serp content (wt%, XRD)		Serp type	Serp polymorph	Average #Mg	Average Al_2O_3 (wt%)	Magnetite
	Mean	Std dev					
Montaut	60	8.9					
			Mesh serp	Ctl-Lz mix	95.0	0.18	✓
			Bastite	Ctl-Lz mix	96.3	2.35	X
			MV1	Ctl-Lz mix	96.7	2.09	✓
			MV2	Ctl-Lz mix	96.1	0.26	X
			MV3	Ctl	96.9	0.4	X
Turon	14	11.8					
			Mesh serp	Ctl-Lz mix	90.9	0.41	X
			Serp vein	Ctl-Lz mix	91.0	1.95	X
Urdach oph	50	1.3					
			Mesh serp	Ctl-Lz mix	92.6	2.59	✓
			Bastite	Ctl-Lz mix	90.9	5.54	X
			Serp veins	Ctl-Lz mix	92.0	3.61	✓
			UV4	Ctl-Lz submicroscopic	97.0	0.48	X
Urdach serpt	99	0.9					
			Mesh serp	Ctl-Lz mix	90.0	1.76	X
			Bastite	Ctl-Lz mix	89.4	5.19	X

Oph = Ophicalcite; Serpt = Serpentinite.
Serp = Serpentine.
Ctl = Chrysotile; Lz = Lizardite.

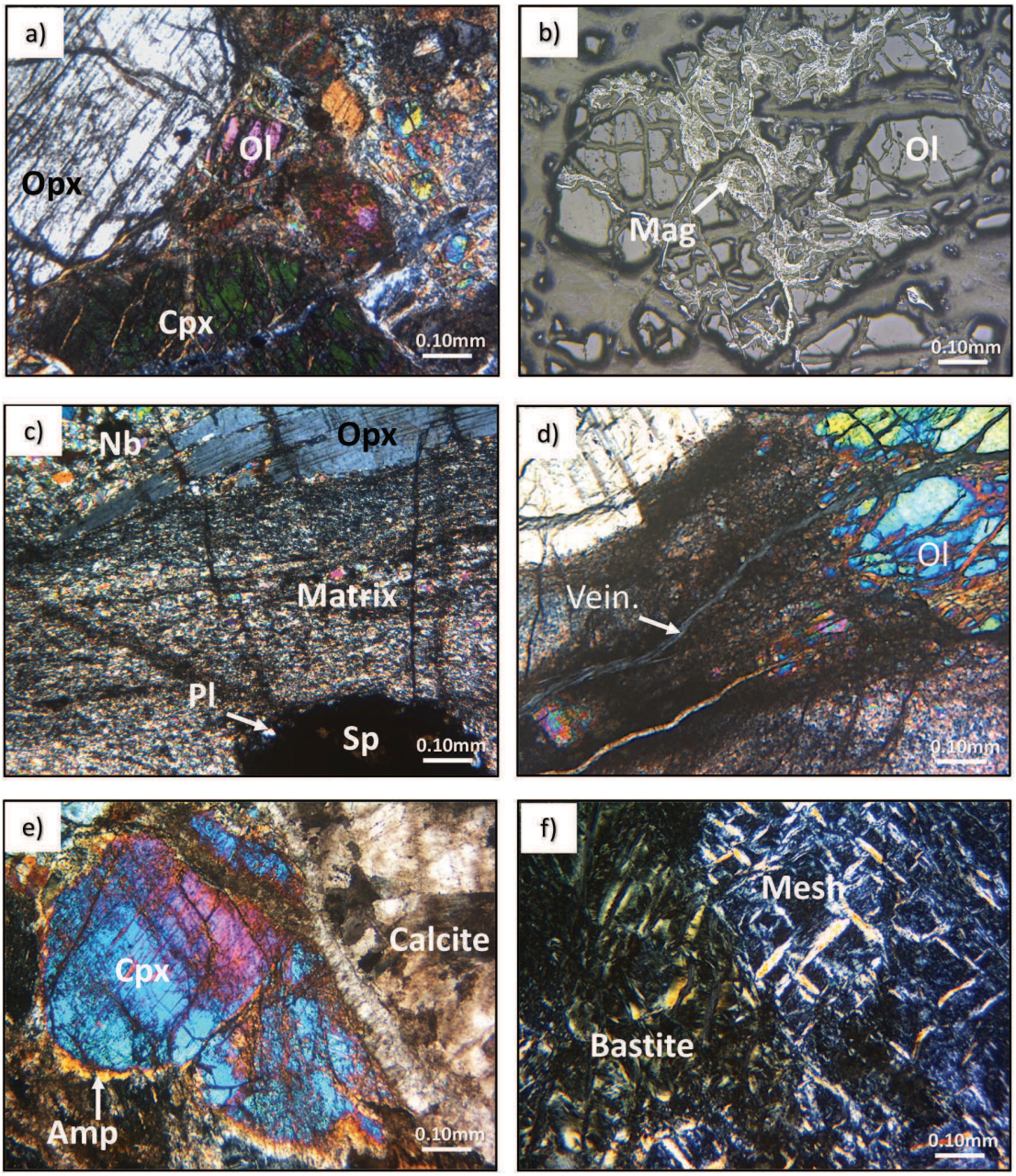

Fig. 2. Representative mineralogy and textures of the studied peridotites. a) Orthopyroxene (Opx), clinopyroxene (Cpx) and olivine (Ol) - Montaut lherzolite MP04 (crossed polars). b) Magnetite (Mag) in mesh serpentine - Montaut lherzolite MP01 (reflected light). c) Turon mylonite TT6, (crossed polars) with elongated Opx porphyroclasts and associated neoblasts (Nb) and partially altered spinel (Sp) in plagioclase (Pl). Minerals in the fine-grained matrix (Matrix) are non-identifiable using microscopy. d) Mesh serpentine with olivine relics (Ol) and serpentine veins (Vein.), Turon protomylonite TT5 (crossed polars). e) Clinopyroxene (Cpx) with amphibole aureole (Amp) - Urdach ophicalcite OU1 (crossed polars). f) Typical mesh serpentine and bastite textures - Urdach serpentinite TU6 (crossed polars).

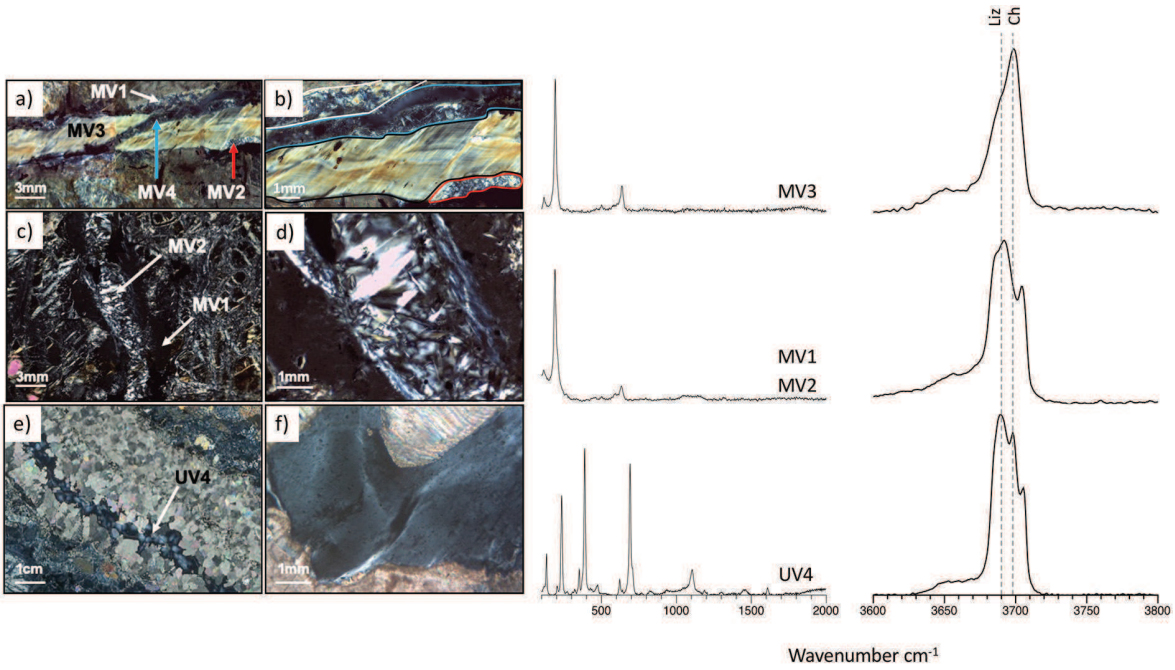

Fig. 3. Serpentine veins from the Montaut massif and Urdach ophicalcite (crossed polars) with associated Raman spectra a) Veins MV1 to MV4 with cross-cutting relationships - lherzolite MP01, Montaut. b) Zoom on MV3 and MV4 veins: banded veins MV3 are parallel to MV1 and MV2. c) Veins MV1 and MV2 in lherzolite MP05, Montaut. MV1 displays a granular texture. Magnetite-rich MV2 is parallel to MV1. d) Zoom on fiber texture of MV2. f) Submicroscopic UV4 vein, cross-cutting a calcite vein - ophicalcite OU1, Urdach. g) Zoom on UV4. On Raman spectra Liz is lizardite and Ch is chrysotile.

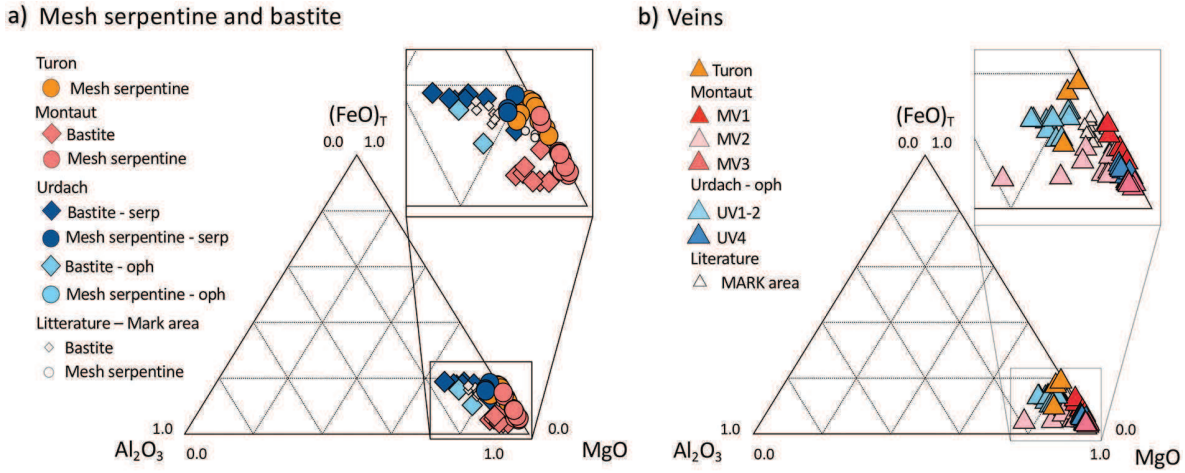

Fig. 4. Al_2O_3-FeO-MgO normalized ternary diagrams with the compositions of a) mesh serpentine and bastite, and b) serpentine veins. Al_2O_3, MgO and FeO contents are considered as equal to 1 to recalculate the proportion of Al_2O_3, MgO and FeO. All Fe is reported as FeO. Data from the oceanic MARK area (Andreani et al., 2007) are reported for comparison.

Four types of serpentine veins were identified, namely MV1, MV2, MV3 and MV4 (Fig. 3). MV1 veins are few cm-size in length and 1 to 6 mm wide (Fig. 3a-b); they have a granular texture. MV2 veins are 3 mm wide, bordered by magnetite; they have a fiber texture. MV1 and MV2 veins are composed of a lizardite-chrysotile mixture. MV3 veins are 3 mm wide magnetite-rich banded veins (banding parallel to vein edges; Fig. 3a-b). They are the only pure chrysotile veins identified. Their structure and morphology indicate a formation by extension or extensional shearing during serpentinization (Andreani et al., 2004). The veins MV1, MV2, MV3 are subparallel to each other, but MV3 locally crosscuts the MV1 and MV2 veins (Fig. 3d-e). All are cross-cut by MV4 veins (Fig. 3a-b). The MV4 veins were too thin (<0.5 μm) to be analyzed.

Olivine has forsterite contents of 89.8 ± 0.3 and NiO concentrations of 0.38 ± 0.03 wt%. Orthopyroxene (Opx) is enstatite with Mg# of 89.6 ± 0.1 and Al_2O_3 concentrations of 3.3 ± 0.2 wt%. Cpx is Cr-diopside (0.74 ± 0.06 wt% Cr_2O_3) with compositions in CaO, Na_2O and TiO_2 of 22.6 ± 0.1 wt%, 1.14 ± 0.04 wt% and 0.10 ± 0.01 wt%, respectively. Spinel is enriched in Al (Cr# = 13.6 ± 1.4). This relatively narrow range of compositions overlaps with the compositions of WP fertile peridotites. Amphibole is Ti-rich tremolite (TiO_2 = 1.90 wt%). Mesh serpentines and bastites have variable compositions compared to the primary minerals after which they formed. Mesh serpentines and bastites have Mg# of 91.9–97 and 94.6–97.6, respectively. Bastites are distinguished from mesh serpentines by their high Al_2O_3 content (>1.19 wt% and < 0.47 wt %, respectively) (Fig. 4a). The composition of vein serpentines overlaps that of the mesh serpentines and bastites, but is more variable (Fig. 4b). The MV1 and MV2 veins have high Mg# values (94.8–97.7 and 92.9–97.7, respectively) compared to mesh serpentines and bastites, and

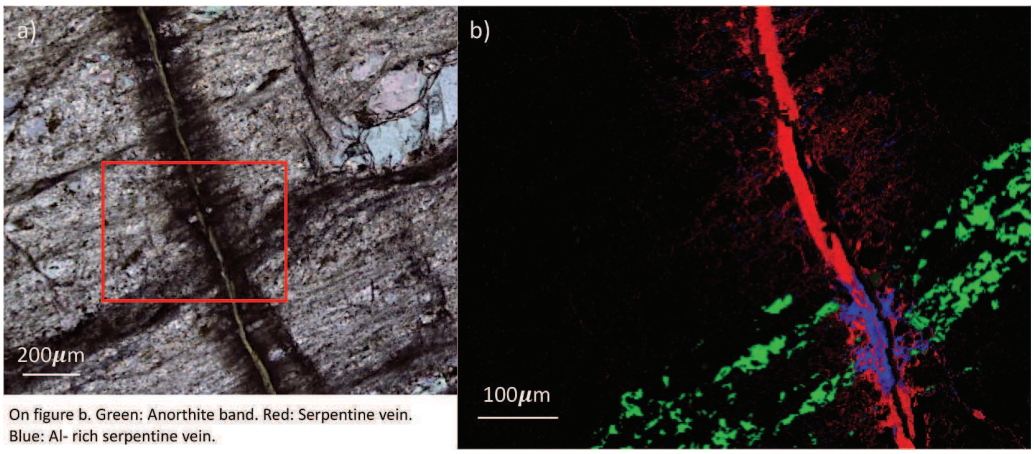

Fig. 5. a) Serpentine vein of the Turon massif (crossed polars). The red frame corresponds to the area used for EPMA mapping. b) Reconstructed phase map of serpentine vein crosscutting plagioclase (Matlab process of EPMA data (Muñoz et al., 2008)). The composition of the vein varies from Mg-rich (in red) to Al-rich (in blue), where plagioclase (in green) is cross-cut. The rim of the serpentine vein displays a fringe geometry. (For interpretation of the references to colour in this figure legend, the reader is referred to the web version of this article.)

the MV3 chrysotile veins display the highest Mg# values (95.5–98.0). MV1 veins are characterized by scattered Al_2O_3 concentrations (0.21–9.07 wt%) compared to mesh serpentines and bastites, and to MV2 and MV3 veins (0.03–0.65 wt% and 0.10–0.68 wt%, respectively).

ii) Turon massif.

The Turon mylonites are spinel and plagioclase bearing lherzolites with the exception of amphibole-bearing harzburgite TT11 (2 wt% Cpx). The direction of mylonitic foliation is N140–160 (Fig. 1d). It is defined in the field by elongated porphyroclasts of Opx, Cpx and spinel and by dark bands of fine-grained matrix in thin sections (Fig. 2c). Plagioclase fraction increases with increasing mylonitization (2 wt% in protomylonites up to 7 wt% in ultramylonites). The occurrence of plagioclase is limited to spinel rims in protomylonites (Fig. 2c) while bands of plagioclase are observed in the fine-grained matrix of ultramylonites (Fig. 5). The Turon lherzolites are poorly to moderately serpentinized (2–32 wt% serpentine), with mesh serpentine developing after olivine (Fig. 2d). The fraction of serpentine depends on the olivine content of the protolith. In the three mylonitic domains, we observed ubiquitous 10 μm thick microfractures oriented nearly perpendicular to foliation (Fig. 2d). They display a fringe geometry corresponding to serpentine developing laterally along the grain boundaries of the fine-grained matrix (Fig. 5). Mesh and vein serpentines are composed of mixed lizardite-chrysotile. Bastite, magnetite, and brucite are not observed.

Olivine has a forsterite content of Fo 89.5 ± 0.3% and NiO concentrations of 0.37 ± 0.06 wt%, similar to the samples from Montaut. In contrast, the composition of pyroxenes varies significantly at the cm scale. Opx is enstatite with Mg# decreasing from 89.7 ± 0.2 in porphyroclasts to 89.2 ± 0.2 in neoblasts. The Al_2O_3 composition of Opx decreases, from core to rim in porphyroclasts (5.1 ± 0.3 wt% to 3.8 ± 0.6 wt%) to neoblasts (0.7 ± 0.3 wt%), while TiO_2 and Cr_2O_3 compositions show similar trends. Cpx is Cr-diopside with CaO, Cr_2O_3 and TiO_2 compositions ranging within 20.2–24.1 wt%, 0.54–2.49 wt% and 0.64–1.28 wt%, respectively; the highest Cr and Ti values being in neoblasts. The Al_2O_3 and Na_2O compositions of Cpx decrease from porphyroclasts cores (Al_2O_3 = 7.3–7.6 wt%; Na_2O = 1.6–2.1 wt%) to rim (Al_2O_3 = 6.7–7.0 wt%; Na_2O = 1.3–2.2 wt%) to neoblasts (Al_2O_3 = 2.4–4.3 wt%; Na_2O = 0.8–1.9 wt%). Spinel is Cr-rich (Cr# = 27.8–32.2) compared to the Montaut samples. The composition of plagioclase is An45 with Cr_2O_3 of 0.14–0.43 wt%. The distinctive compositions of Opx and Cpx neoblasts, in particular their low Na and Al contents, is associated to the sub-solidus replacement of spinel by plagioclase (Fabriès et al., 1998).

Serpentines are Fe-rich compared to the Montaut mesh serpentines with Mg# values of 89.9–93.2 in mesh serpentines and 88.4–94.6 in veins (Fig. 4a). The composition of veins varies with the crosscut lithologies. In particular, the composition of serpentines becomes Al-rich (blue-colored parts in Fig. 5b) when cross-cutting plagioclase bands, with Al_2O_3 concentrations up to 3.75 wt% compared to 0.01–1.85 wt% in mesh serpentines.

iii) Urdach massif

The samples from Urdach are dominantly spinel lherzolites. They underwent high degrees of serpentinization and, locally, carbonation. Two domains are distinguished: the completely serpentinized peridotites (100 wt% serpentine) at the center of the massif and ophicalcites (50–55 wt% serpentine). Only ophicalcites preserve the primary coarse-grained texture of peridotites with rare relics (~ 0.5 mm) of olivine, orthopyroxene and clinopyroxene.

In ophicalcites, mesh serpentine and bastite develop after olivine and pyroxenes, respectively. Mesh serpentine is marked by an alignment of magnetite along mesh veins (1–4 wt% magnetite). Pyroxenes are less altered than olivine; showing fresh cores with bastite rims (Fig. 2e). Spinel rims are altered to ferrichromite. Amphibole (actinolite) forming after pyroxenes is observed in ophicalcite (OU1 sample; Fig. 2e). Four serpentine vein types are distinguished in ophicalcites, namely UV1, UV2, UV3 and UV4. The first three types are identical in texture and morphology to Montaut veins MV1, MV3 and MV4. Vein UV4 grows parallel to a thick calcite vein (~3 cm wide; Fig. 3e-f) and its thickness varies along the calcite vein (0.1 to 2 cm). It exhibits undulating extinction in cross polarized light. It is composed of submicroscopic serpentine, identified as a mix of chrysotile and lizardite (Fig. 3). Serpentinites comprise mesh serpentine and subordinate bastite. They have no magnetite and no veins (Fig. 2f).

Pyroxenes from ophicalcites overlap in composition with the Turon porphyroclasts (cores and rims). Opx is enstatite with Mg# of 89.7 ± 0.3 and variable Al_2O_3 contents (3.23–5.60 wt%). Cpx is Cr-diopside of variable compositions in CaO (18.75–23.85 wt%), Al_2O_3 (6.19–7.92 wt %), Na_2O (1.29–1.87 wt%), Cr_2O_3 (0.75–1.23 wt%) and TiO_2 (0.46–1.50 wt%). Chromium spinel is Cr-poor (Cr# = 9.7) compared to

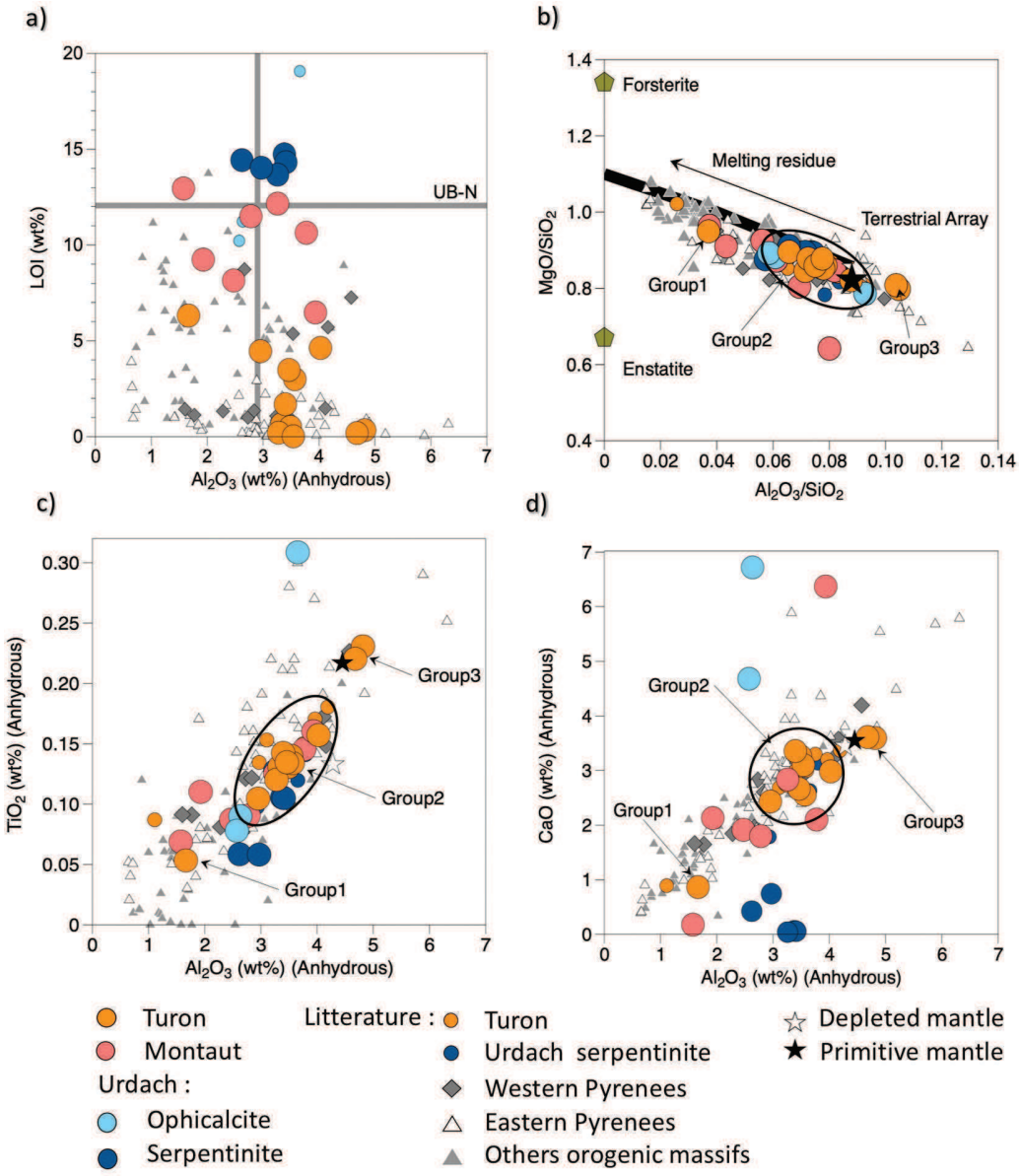

Fig. 6. Bulk rock composition of the Montaut, Turon, and Urdach samples reported on: a) LOI versus Al_2O_3 (wt% anhydrous) b) MgO/SiO_2 versus Al_2O_3/SiO_2 and compared to bulk silicate Earth "terrestrial array" (black line - Hart and Zindler, 1986; Jagoutz et al., 1979). c) TiO_2 (wt% anhydrous), and d) CaO (wt% anhydrous) versus Al_2O_3 (wt% anhydrous). UB-N composition is from Georem (http://georem.mpch-mainz.gwdg.de; date of reading: 06/2020). Compositions of the depleted mantle (DM, blank star) and primitive mantle (PM, black star) are from Salters and Stracke (2004) and McDonough and Sun (1995), respectively. Literature data for Turon and Urdach massifs, and other Pyrenean peridotite massifs are from Bodinier et al. (1988) and Fabriès et al. (1998). Literature data for other orogenic peridotite massifs are from Bodinier et al. (1988); Gueddari et al. (1996); Van der Wal and Bodinier (1996).

Turon and Montaut. Actinolite has variable TiO_2 contents (0.58–4.2 wt %).

Mesh serpentines and bastites in ophicalcites have variable compositions comparable to Montaut and Turon with Mg# in the range of 91.3–95.9 and 89.3–93.8, respectively, and Al_2O_3 contents of 0.68–4.61 wt% and 5.49–5.56 wt%, respectively (Fig. 4a). Mesh serpentines and bastites in serpentinite are slightly Fe-rich compared to ophicalcites with Mg# in the range of 89.4–90.4 and 88.1–92.8, respectively (Fig. 4a), but they have similar Al_2O_3 compositions (1.06–2.14 wt% and 2.41–7.85 wt %, respectively). Serpentine veins UV1 and UV2 have similar compositions, overlapping that of mesh serpentine and bastite (Mg# = 90.7–92.9; Al_2O_3 = 1.87–4.61 wt%; Fig. 4). Serpentine veins UV4 are Fe- and Al-depleted compared to mesh serpentine, bastites and the other serpentine veins (Mg# = 96.4–97.6; Al_2O_3 = 0.60–0.68 wt%; Fig. 4b).

4.2. *Bulk-rock geochemistry*

XRF and ICP-MS results are reported in Supplementary Material Table A4.

4.2.1. *Major elements*

The studied samples overlap in composition with previously analyzed WP and EP peridotites, as illustrated on Fig. 6. They plot close to the differentiation array on the MgO/SiO_2 versus Al_2O_3/SiO_2 diagram (Jagoutz et al., 1979), toward its most fertile end-member, close to Primitive Mantle (PM) values. They are distinguished by their scattered and high LOI compared to EP peridotites (LOI 0–5 wt%).

The peridotites from Montaut have LOI of 6.5–13 wt%. The sample MP07, with the highest LOI, has among the highest serpentine (65 wt%)

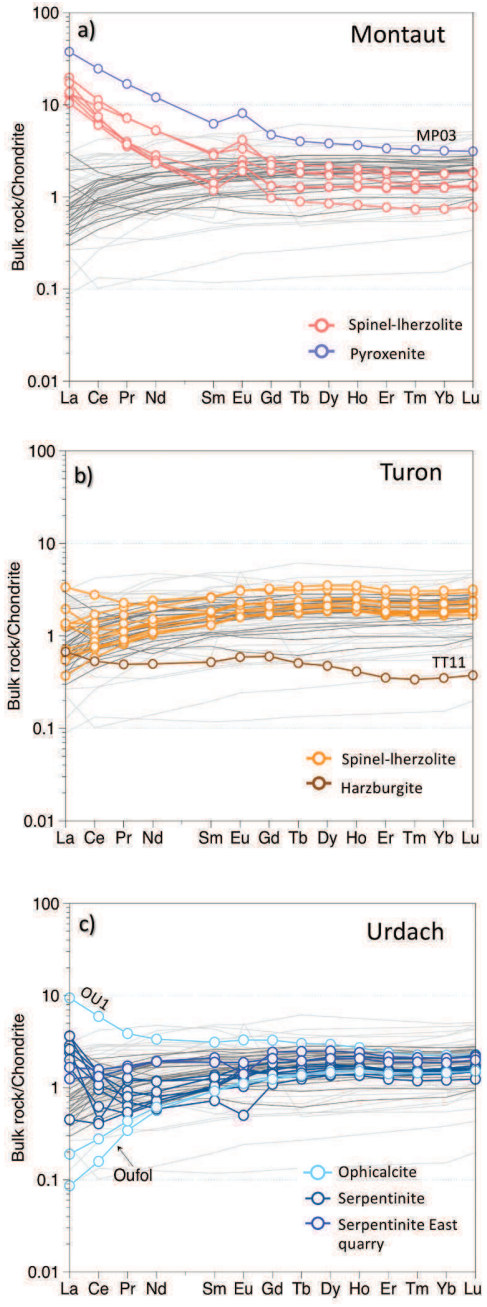

Fig. 7. Bulk rock REE compositions of peridotites from a) the Montaut massif and b) Turon massif and c) Urdach massif. Dark grey and light grey patterns are from other Western and Eastern Pyrenees massifs, respectively (data are after Bodinier et al., 1988, and Fabriès et al., 1998). Chondrite normalizing values are after McDonough and Sun (1995).

and chlorite (27 wt%) contents. Montaut peridotites have fertile compositions consistent with their lherzolitic protolith with Al_2O_3 of 1.37–3.68 wt% (Fig. 6a), TiO_2 of 0.06–0.15 wt% (Fig. 6c) and MgO/SiO_2 ranging between 0.64 for pyroxenite-bearing lherzolite MP03, and 0.80–0.96 for lherzolites (Fig. 6b). Amphibole-bearing lherzolites MP01, MP02 and MP03 have the highest Al_2O_3 and TiO_2 contents. Montaut peridotites display extremely variable CaO (0.2 wt% for weathered sample MP07 and 6.4 wt% for pyroxenite-bearing sample MP03; Fig. 6d). CaO shows no correlation to immobile elements classically used to quantify magmatic processes (e.g., Al_2O_3 and TiO_2).

The Turon peridotites have the lowest LOI (0–6.3 wt%), with the highest value for harzburgite TT11, the most serpentinized sample (Fig. 6a). Three groups are distinguished: harzburgite TT11 with high Mg# (90.5) and low Al_2O_3/SiO_2 values (0.04) and TiO_2 contents (0.05 wt%), lherzolites with Mg# values of 89.4–90, Al_2O_3/SiO_2 of 0.06–0.08, and TiO_2 of 0.10–0.15 wt%, and pyroxenite-bearing lherzolites TT5 and TT12 having low Mg# values (88.3–89.5), and with Al_2O_3/SiO_2 and TiO_2 higher than PM values ($Al_2O_3/SiO_2 = 0.10–0.11$; $TiO_2 = 0.22–0.23$ wt%; Fig. 6b-c). The same trend is observed for CaO (Fig. 6d).

The samples from Urdach have high LOI in the range of 13.7–14.7 wt % for serpentinites and 10.2–19.1 wt% for ophicalcites (Fig. 6a), that reflect their high and variable fractions of serpentine and carbonate. Ophicalcite OU1 that has the highest LOI has also the highest calcite content (31 wt% XRD). The variously carbonated and serpentinized Urdach samples (Fig. 6b) overlap in composition with the Turon lherzolites ($Al_2O_3/SiO_2 = 0.06–0.07$; Mg# = 89.1–90.7; $TiO_2 = 0.05–0.09$ wt%), except for ophicalcite OU1 that has more fertile compositions overlapping with that of Turon pyroxenite-bearing lherzolites ($Al_2O_3/SiO_2 = 0.09$; Mg# = 89.3; $TiO_2 = 0.25$ wt%; Fig. 6b-c). We observe variations in calcium with high CaO in ophicalcites (4.20–14.28 wt%) and low CaO in serpentinites (0.04–0.64 wt%; Fig. 6d).

4.2.2. *Trace elements*

The normalized REE and trace element patterns of peridotites and pyroxenites from Montaut, Turon and Urdach are presented in Fig. 7 and in Supplementary fig. A3. Similar to Pyrenean peridotites analyzed previously (see review of Bodinier and Godard, 2013), the WP peridotites have bulk rock compositions close to PM values for heavy REE (e.g., $Yb_N = 0.8–3$; N = normalized to C1-chondrite (McDonough and Sun, 1995)), except for selective fractionations and enrichments in highly incompatible and fluid mobile elements.

The lherzolites from Montaut are characterized by strong enrichments in Light REE (LREE) relative to Heavy REE (HREE) ($Yb_N = 0.74–3.16$; $(La/Yb)_N = 7–23.3$; Fig. 7a) and positive Eu anomalies ($(Eu/Eu^*) = 1.23–1.77$). Their REE concentrations increase with increasing fraction of Cpx and amphibole: the most enriched sample, labelled MP03, being amphibole-, and Cpx-rich lherzolite. They have patterns similar to that of amphibole-bearing EP peridotites (Bodinier et al., 1988). All samples are also particularly enriched in Ba (Ba/Th = 1.9-18xPM; PM values from McDonough and Sun, 1995), Pb (Pb/Ce = 9-39xPM), and to a lesser extent in U (U/Th = 0.07-4xPM). Zr/Hf is slightly fractionated (19.3–24.7; PM = 36.2) in contrast to Nb/Ta (64–115) that deviates significantly from PM values (17.4; see Supplementary Fig. A3).

Turon lherzolites have LREE-depleted patterns typical of fertile lherzolites ($Yb_N = 1.66–3.08$; $(La/Yb)_N = 0.21–0.57$; Fig. 7b), except for lherzolites TT1 and TT10 that show selective enrichments in LREE ($(La/Nd)_N = 1.50–1.59$). TT11 harzburgite is HREE depleted compared to lherzolites and display a relatively flat pattern ($Yb_N = 0.35$; $(La/Yb)_N = 1.93$). All samples are selectively enriched in Rb and Ba (Rb/Th = 1.1-42xPM; Ba/Th = 0.96-365xPM), Pb (Pb/Ce = 17-129xPM) and to a lesser extent in U and Sr (U/Th = 1.3-16xPM, Sr/Ce = 1.2–4.7xPM). Zr/Hf and Nb/Ta are low to comparable to PM values (27–31.9 and 6.4–18 respectively; see Supplementary Fig. A3).

Urdach lherzolites are characterized by flat HREE segments and variable LREE fractionation ($Yb_N = 1.21–2.25$; $(La/Yb)_N = 0.06–4.2$; Fig. 7c). LREE-enriched samples comprise ophicalcite OU1 ($(La/Yb)_N = 4.2$) and west quarry serpentinites ($(La/Sm)_N = 1.6–4$). Serpentinites are distinguished from ophicalcites by their variable Eu anomalies ($Eu/Eu^* = 0.56–1.32$). All samples show a particular enrichment in Rb and Ba (Rb/Th = 0.4 - 445xPM; Ba/Th = 1.6-94xPM), Pb (Pb/Ce = 2 -200xPM) and U and Sr (U/Th = 9.2-131xPM, Sr/Ce = 0.2-20xPM; see Supplementary Fig. A3). The highest Sr values were measured in ophicalcites. Zr/Hf overlaps with the Turon peridotite values (20–31.9). In contrast, Nb/Ta is highly variable, with values close to PM in ophicalcites (14.5–18.3) and highly scattered in serpentinites (6.4–107.6).

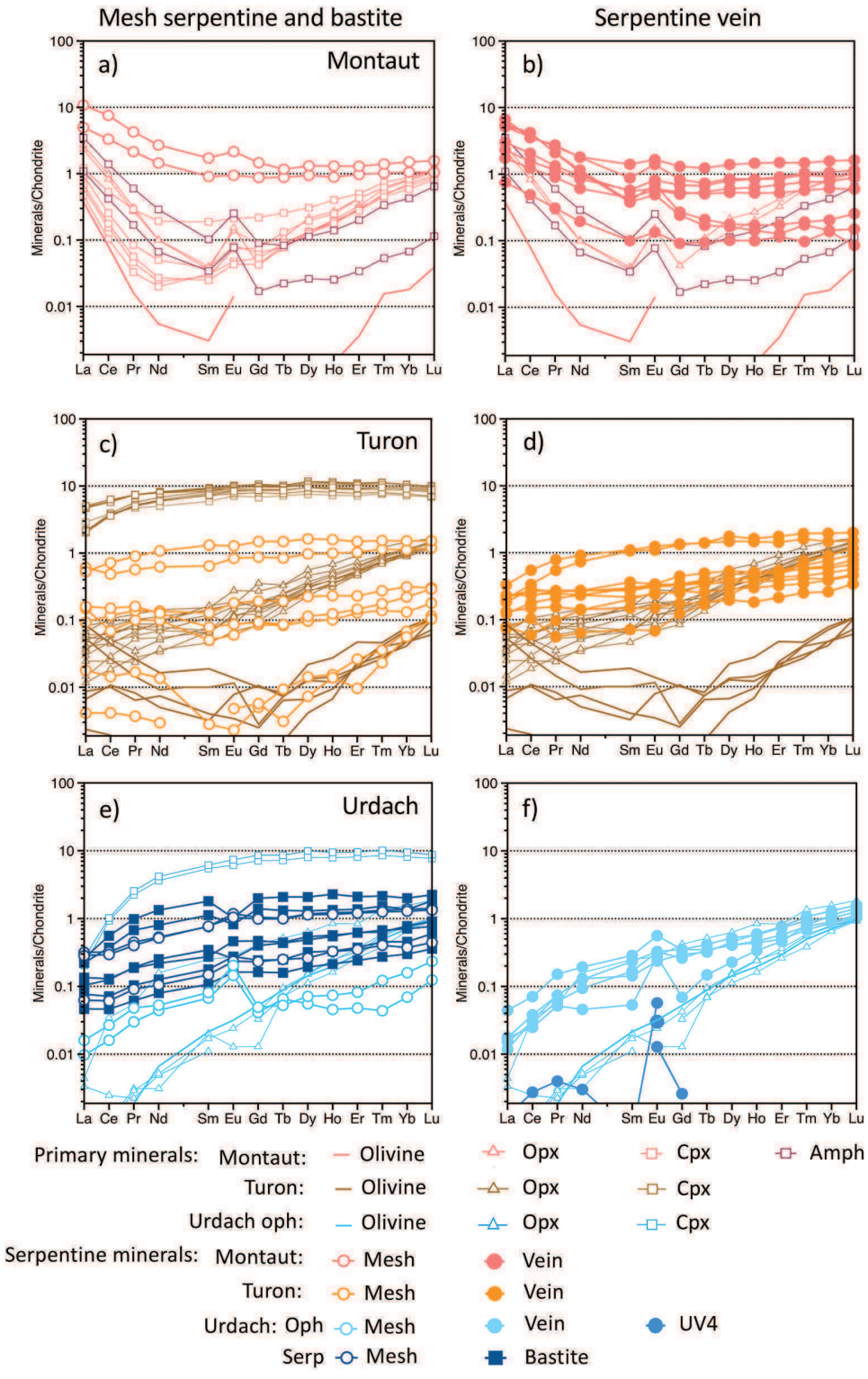

Fig. 8. REE patterns for serpentine phases after olivine (mesh serpentine), pyroxene (bastite), and in serpentine vein for a) and b) Montaut massif, c) and d) Turon massif and e) and f) Urdach massif. Primary minerals, i.e., olivine, amphibole, orthopyroxene and clinopyroxene REE compositions are shown for comparison.

4.3. Trace element composition of serpentine phases

LA-ICP-MS results are reported in Supplementary Material Table A5. The compositions measured in mesh serpentine and bastite for elements commonly considered as fluid immobile (e.g., REE) are comparable to that of the primary minerals after which they were formed: olivine, pyroxenes, and possibly amphibole for the Montaut samples (e.g., Fig. 8). The mesh serpentine of Turon and Urdach massifs is characterized by flat patterns with a slight depletion in LREE. Mesh serpentine of Montaut massif is characterized by LREE-enriched patterns identical to primary minerals and amphibole patterns. Urdach bastites have intermediate compositions between Opx and Cpx and REE patterns similar to

Table 2
Summary of the temperature estimates for the three massifs.

		T two pyroxene [1] (°C)		TCa in Opx [2] (°C)		T in REE [3] (°C)	
	Texture	#	Range	#	Range	#	Range
Montaut							
MP04	Core	–	–	*n* = 9	794–934	–	–
MP05	Core	–	–	n = 4	798–898	–	–
Turon							
TT1	Porphyroclast core	*n* = 2	848–860	n = 2	954–1003	n = 2	1043–1120
	Neoblast	n = 2	826–832	n = 2	765–779		–
TT3	Porphyroclast core	n = 1	737	n = 4	921–1065	n = 1	911
	Neoblast	–	–	n = 4	700–849		–
Urdach							
OU	Core	–	–	n = 2	871–913	–	–
Oufol	Core	–	–	n = 9	820–925	–	–

[1] Wells (1977) and Brey and Köhler (1990).
[2] Brey and Köhler (1990).
[3] Liang et al. (2013).

mesh serpentine. The composition of vein serpentines is generally similar to that of mesh serpentines, attesting of low element mobility at the sample scale during serpentinization. Only the late UV4 veins in Urdach ophicalcites have distinctive compositions, with low values in REE and highly to moderately incompatible elements (Fig. 8f). Mesh serpentine, bastite and vein serpentine display variable and enriched compositions in fluid mobile elements (FME) such as Pb, Sb, or Li, although some minerals can overlap in compositions with olivine, pyroxenes and amphibole.

4.4. Geothermobarometry

Temperatures are reported in Supplementary Material Table A6 and summarized in Table 2. For the protomylonite samples from Turon, the pressure is 500 ± 0.06 MPa, which is consistent with the previous estimates by Fabriès et al. (1998) and Vissers et al. (1997). Temperatures determined in the porphyroclast cores range between 911 and 1120 °C, 921–1065° and 737–860 °C using the T_{REE}, $T_{Ca\text{-}in\text{-}Opx}$ and $T_{2\text{-}Px}$ thermometers, respectively. The temperatures obtained for neoblasts are lower, showing ranges between 700 and 849 °C and 826–832 °C using the $T_{Ca\text{-}in\text{-}Opx}$ and $T_{2\text{-}Px}$ thermometers, respectively. The temperatures using the three thermometers overlap suggesting a progressive cooling of the Turon peridotite. The decrease of crystallization temperatures from porphyroclasts to neoblasts is interpreted by Fabriès et al. (1998) and Vissers et al. (1997) as evidence that mylonitization occurred during this cooling history, likely in association to tectonic exhumation.

Because of their high degree of alteration of the Montaut and Urdach samples, we used only the $T_{Ca\text{-}in\text{-}Opx}$ thermometer to calculate equilibrium temperatures. Based on the results of Fabriès et al. (1998), the equilibration pressure was set at 1 GPa for these calculations. Temperatures were determined on two peridotites from Montaut (794–898 °C) and two ophicalcites from Urdach (820–925 °C). These values are consistent with previous temperature estimates from these two peridotite massifs (Fabriès et al., 1998).

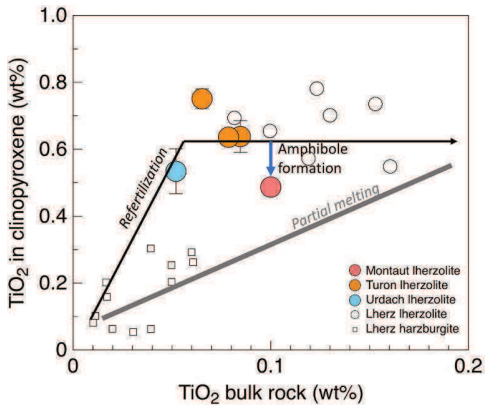

Fig. 9. Cpx TiO_2 versus bulk rock TiO_2 compositions in the WP peridotites, compared to the compositions of the peridotites from the Lherz massif (Le Roux et al., 2007).

5. Discussion

5.1. The Western Pyrenees peridotite massifs: Sampling the transition from continental lithosphere to mantle exhumed at a distal passive margin

The variously serpentinized peridotites from the Montaut, Turon and Urdach massifs preserve part of their primary petrographic and geochemical mantle signatures, thus providing some insights on the nature of their mantle protoliths. It should be noted however that the high degree of hydrothermal alteration of the Montaut and Urdach massifs hindered a comprehensive study of primary textures and mineral compositions to determine precisely the petrogenetic processes undergone by the three massifs, in particular their geothermobarometric pathways.

The studied samples, representative of the three massifs, are lherzolites and Cpx-rich and/or pyroxenite-bearing lherzolites, with minor harzburgite (one sample from Turon). Except for fluid mobile and highly incompatible elements (for which there is little data for comparison), their major and trace element bulk and mineral compositions plot within the compositional fields defined by the previously analyzed WP and EP peridotites (e.g., Fig. 6-7) (Bodinier et al., 1988; Fabriès et al., 1991; Fabriès et al., 1998). The analyses available, although limited, indicate that lherzolites (± Cpx) were formed by refertilization as proposed by Le Roux et al. (2007) for the peridotites of the Lherz massif, one of the most studied EP massifs. First, the studied suite of lherzolites (± Cpx) shows the same covariations in major, minor and trace element compositions as the refertilized lherzolites from Lherz. Second, Ti content of Cpx was constant when Ti content in bulk rock varied (Fig. 9), traducing a geochemical signature typical of refertilization reactions. These results imply that the WP peridotites sampled the same protolith as the EP peridotites, which was likely a variously refertilized subcontinental lithospheric mantle (e.g., Bodinier and Godard, 2013). However, as first emphasized by Fabriès et al. (1998), the WP peridotites are distinguished by a predominance of fertile lithologies compared to the EP peridotites. This difference is interpreted as related to their two-step uplift and cooling history during Cretaceous extension (Fabriès et al., 1998; Lagabrielle et al., 2019a; Lagabrielle et al., 2019b). During the first stages of lithospheric thinning and tectonic exhumation, isothermal decompression favored extensive melt-rock interactions at the upward moving lithosphere-asthenosphere boundary. The late fast cooling

episode associated to mantle uplift and exhumation to shallow depths resulted in trapping of infiltrating melts and the development of melt impregnation textures, a common feature in peridotites from fossil and active OCTs (e.g., Iberian margin (Hébert et al., 2001); Australian-Antarctic margin (McCarthy et al., 2020); Lower Platta (Muntener et al., 2009)). These complex uplift and cooling processes produce variable petrogenetic pathways for peridotites, depending on their localization along the exhumed lithospheric mantle, resulting in differences in structure, mineralogy and geochemistry as recorded by Montaut, Turon and Urdach peridotites.

The Montaut peridotites display equilibration temperatures similar to those reported for the subcontinental lithospheric mantle in the EP and WP peridotites (~900 °C, ~1GPa; Fabriès et al., 1998; Fabriès et al., 1991). They are distinguished by abundant mineralogical and geochemical evidences of fluid-rock interactions taking place over a broad range of temperatures. The abundance of tremolite, talc, serpentine and clays and the selective bulk enrichments in FME indicate that these reactions were dominantly hydrothermal to weathering reactions as discussed in chapter 5.2. However, these hydrothermal processes cannot account for the characteristic Ti- and LREE-rich compositions of the Montaut peridotites and, in particular, their strong Nb—Ta fractionation. These compositions are similar to those observed in the metasomatized EP peridotites close to high temperature amphibole dikes (typically Ti-pargasite), that reveal interactions with alkali basalts and volatile-rich melts during the earliest stages of continental thinning (Downes et al., 1991). These geochemical characteristics suggest that the Montaut peridotites underwent a similar episode of mantle metasomatism, previous to hydrothermal alteration and weathering.

The Turon peridotites preserve evidence of high stress mylonitic deformation, occurring during the second stage of uplift that distinguishes the WP peridotite massifs from their EP counterparts. Geothermobarometry indicates cooling from more than 1000 °C (protomylonites) down to 700 °C (ultramylonites) and the presence of subsolidus plagioclase at the rim of spinels indicates tectonic exhumation with peridotite equilibration at shallow depths (~0.5 GPa) (Fabriès et al., 1998; Vissers et al., 1997). Nevertheless, in contrast to the peridotites from the Montaut massif, the Turon peridotites were little to not modified by hydrothermal alteration (no evidence of amphibole, low degree of serpentinization).

The Urdach peridotites are highly altered: they comprise mainly serpentinites and ophicalcites. They preserve too little relics of primary minerals to reconstruct their petrogenesis before hydrothermal alteration but structural reconstructions provide evidence that the massif was exhumed onto the seafloor during the mid-Cretaceous extension before burial below *syn*- and post-rift sediments (e.g., Clerc et al., 2013; Lagabrielle et al., 2010). Serpentinites and ophicalcites are exposed along a complex system of extensional detachment faults inverted during the Pyrenean compression (Lagabrielle et al., 2019b). These structural features probably acted as main fluid pathways during mantle exhumation and tectonic emplacement.

The contrasted structural and petrological characteristics of the Montaut, Turon and Urdach massifs reflect their geological environment along the embryonic passive margin during mid-Cretaceous extension and lithosphere thinning (Lagabrielle et al., 2010), with the Urdach peridotites directly exposed to the seafloor in the most distal (basinward) domain whilst the Montaut peridotite massif remained below a 200 m-thick unit of continental upper crust (Devonian metasediments) and thus correspond to a more internal domain. The Turon peridotites, which occur directly below the Mesozoic pre-rift cover, would represent an intermediate domain in this extensional system. Thereafter, we combine our mineralogical observations on secondary minerals and our new geochemical dataset with structural considerations to better constrain the mechanisms driving the hydrothermal reactions modifying the WP peridotites and the geological environments in which they occurred.

5.2. *Variability in serpentinization conditions in the Western Pyrenees peridotites*

i) *Turon massif*

The peridotites from the Turon massif are the least serpentinized peridotites from the WP peridotites, and mainly contain primary mantle minerals. They contain minor amounts of serpentine and no magnetite. Serpentinization is a hydration reaction that requires the development of fluid pathways from the massif to the mineral scale to allow fluid access at the mineral interfaces (e.g., Escario et al., 2018; Godard et al., 2013; Malvoisin et al., 2012). The Turon massif was emplaced along a diapiric zone of Upper Triassic Keuper facies reactivated as a thrust during tectonic inversion but no faults and fractures are observed to crosscut the massif thus limiting fluid infiltration, and therefore serpentinization. Only a few fine serpentine-filled cracks are observed, perpendicular to foliation, in the most serpentinized samples (Fig. 5). These sparse fine veinlets likely acted as the only fluid pathways for serpentinizing fluids in the low-permeability Turon peridotites. They have compositions influenced by the surrounding primary minerals (Fig. 5) indicative of a rock-dominated reactive system and thus of low fluid input. By limiting precipitation of the low-density serpentines, these low flow conditions during the onset of serpentinization likely precluded reaction-driven cracking (e.g., Plümper et al., 2012) commonly envisaged as an important process for maintaining permeability during serpentinization.

In spite of their limited degree of alteration, the bulk rock composition of the Turon peridotites is characterized by selective enrichments in FME (Li, Sb, As, Cs, Rb, Ba and Pb) when compared to the EP peridotites (here represented by the Lherz massif, the only EP peridotite massif for which the trace element database is complete, Fig. 10a) and to Depleted Mantle (DM) and PM values (Fig. 11a). This chemical signature suggests interactions with fluids. It differs from that of oceanic serpentinites, which is characterized by strong U enrichments produced by interactions with oxidizing seawater-derived fluids (Deschamps et al., 2012; Deschamps et al., 2013; Kodolányi et al., 2012; Paulick et al., 2006; Peters et al., 2017). The FME composition of the Turon peridotites overlaps that of neighboring metasediments (Li, As, Sb, Pb) or is intermediate between PM values and sediment compositions (Cs) and, except for Ba, they are mostly hosted by serpentine (Fig. 11a). This suggests that the FME-rich fluids triggering serpentinization in the Turon peridotites derived mainly from neighboring sediments or from lithologies having similar compositions.

ii) *Montaut massif*

The Montaut peridotites record successive episodes of hydrothermal alteration over a broad range of decreasing temperatures. The first stage of the hydrothermal alteration is characterized by the formation of the tremolite, talc and chlorite assemblage, to which is closely associated

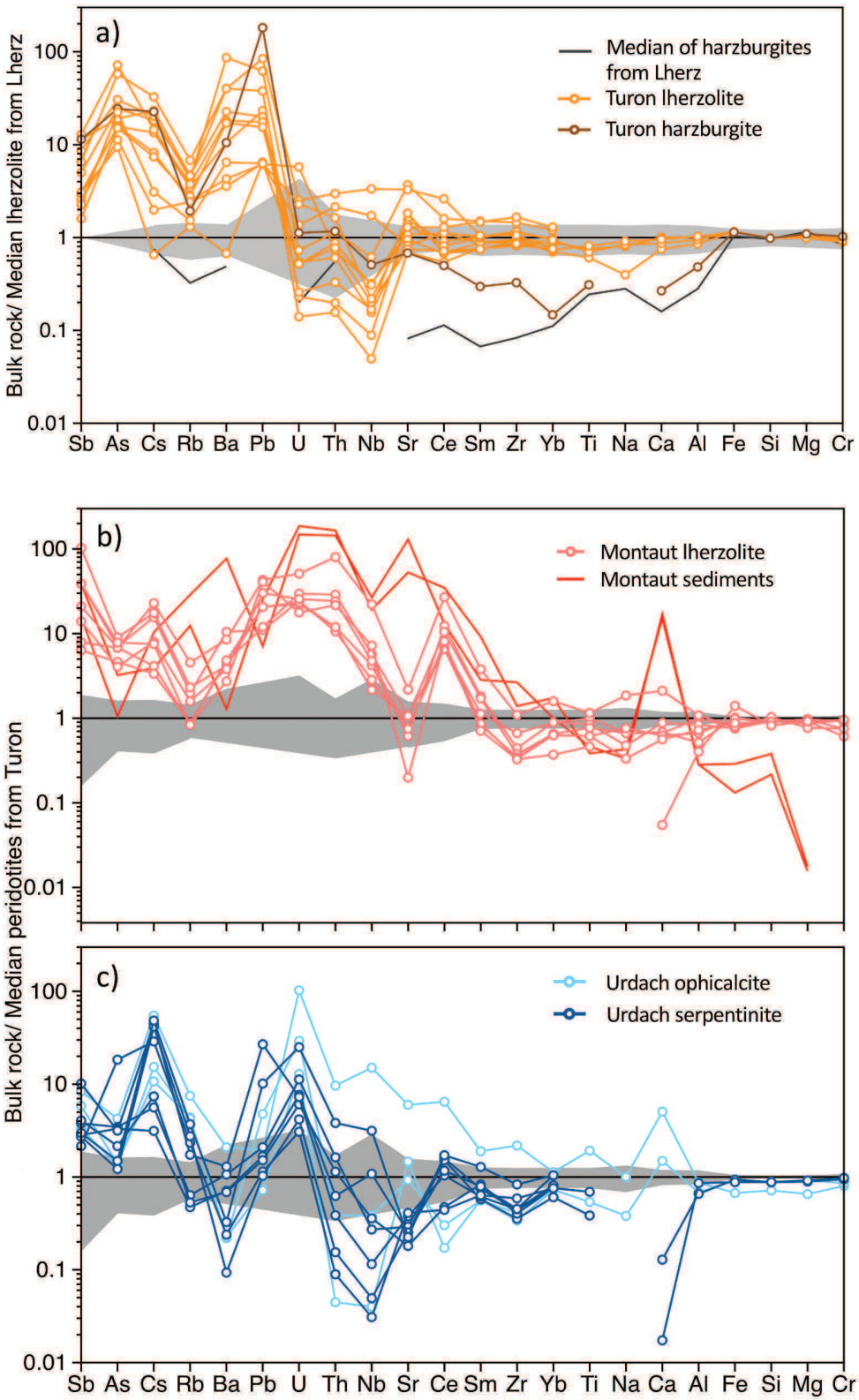

Fig. 10. Major, minor and trace element patterns of a) Turon lherzolites normalized to the median of Lherz lherzolites after Le Roux et al. (2007). The grey box represents the median ± the median absolute deviation of Lherz lherzolites. b) Montaut lherzolites normalized to the median of Turon lherzolites. Red solid lines represent the associated sediments. The grey box represents the median ± the median absolute deviation of Turon lherzolites. c) Urdach lherzolites (i.e., serpentinites in dark blue and ophicalcites in light blue) normalized to the median of Turon lherzolites. The grey box represents the median ± the median absolute deviation of Turon lherzolites. (For interpretation of the references to colour in this figure legend, the reader is referred to the web version of this article.)

serpentine and magnetite. Similar mineral assemblages are commonly observed in peridotites exhumed along detachment faults from slow spreading ridges; they are interpreted as characterizing incipient high temperature serpentinization that affects mostly pyroxenes (350–450 °C up to ~550 °C; Bach et al., 2004; Rouméjon et al., 2018). Samples from Montaut are crosscut by successive generations of serpentine veins, with textures indicative of formation in extension or extensional shearing conditions, these features being the most prominent in the late banded veins (Andreani et al., 2004) (Fig. 3a-b). These veins record also changes in chemistry indicating an evolution in serpentinization conditions over

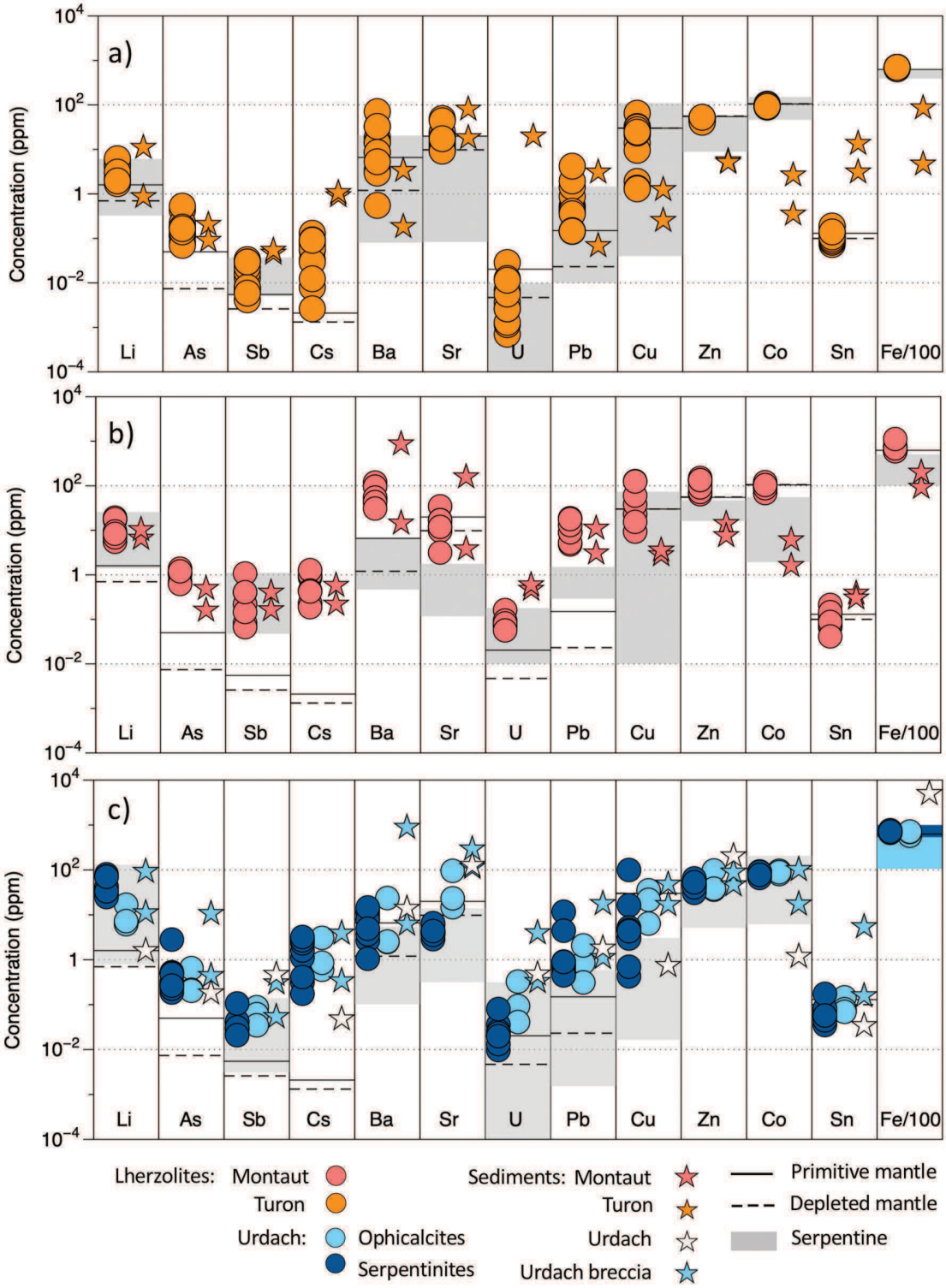

Fig. 11. Plots of concentrations of selected fluid-mobile elements (Li, As, Sb, Cs, Ba, Sr, U, and Pb), metals (Cu, Zn, Co and Sn) and Fe/100 of peridotites and associated sediments from a) Turon, b) Montaut and c) Urdach. Solid and dotted lines represent PM (McDonough and Sun, 1995) and DM (Salters and Stracke, 2004) values respectively. Grey boxes represent the range of each fluid-mobile element measured in serpentine phases. Light blue box in the Fe/100 column represents the range measured in serpentine phases of Urdach ophicalcites while dark blue box represents the range measured in serpentine phases of Urdach serpentinites. (For interpretation of the references to colour in this figure legend, the reader is referred to the web version of this article.)

time (temperature, fluid flow and/or composition; Fig. 4b). We suppose that the extensive alteration of Montaut peridotites was facilitated by their proximity to a major fault system, the NPFT, that likely inverted an extensional detachment of the rift system. This fault may have acted as a major fluid pathway from the earliest stages of cooling during tectonic exhumation.

Montaut peridotites are characterized by strong enrichments in FME compared to the EP and Turon peridotites (Fig. 10b), and to DM and PM values (Fig. 11b), indicative of intense hydrothermal activity. They overlap in composition with neighboring sediments for LREE (Fig. 10b) and for most FME (e.g., Li, As, Sb, Ba, Cs, Sr, Pb; Fig. 11b). Li, Sb and U are carried by serpentine (Fig. 11b). Sulfide and oxide microphases likely play a significant role in the redistribution of other FME, such as Ba and Pb, and metals (Co, Ni, Zn, Sn) (Deschamps et al., 2012). Another characteristic is the occurrence of Eu positive anomalies in the absence of plagioclase. This anomaly typically develops in reducing conditions during serpentinization when triggered by low pH, high temperature (>300 °C), and high chlorinity fluids (e.g., Paulick et al., 2006). Serpentinization likely resulted from interactions with fluids derived from neighboring sediments with possible changes in salinity and pH associated with fluid-rock interactions.

iii*) Urdach massif*

The peridotites from Urdach are almost completely altered to ophicalcites (serpentine, calcite and magnetite) and serpentinites (dominantly serpentine). Previous studies (Clerc et al., 2013; Lagabrielle et al., 2010; Lagabrielle et al., 2019b) have substantiated that the serpentinization and carbonation reactions occurred as the cooling hyperextended mantle was tectonically exposed at or near the seafloor. The formation of calcite veins characterizes the final stages of this process; it occurred in a still hot (200–230 °C) environment and reveal chemical interactions with seawater-derived hydrothermal fluids (Corre et al., 2018; DeFelipe et al., 2017). The formation of submicroscopic Mg-rich - REE-depleted serpentine veins is commonly associated to these veins (Fig. 3e) suggesting that serpentinization and carbonation reactions were contemporaneous down to low temperatures.

Serpentinites and ophicalcites from Urdach are enriched in FME, including U as expected for oceanic serpentinization (Fig. 10c). They show also high Cs, Pb, As and Sb concentrations similar to that of neighboring sediments deposited above the peridotite massif, suggesting interactions with sediment-derived fluids triggered by tectonic exhumation and possibly continuing during sedimentary burial. Most of the FME are concentrated in serpentine and have similar compositions in serpentinites and ophicalcites, except for Li that is selectively enriched in serpentinites (6–17 ppm in ophicalcites and > 25 ppm for serpentinites), suggesting a stronger siliciclastic component in the fluid source (Fig. 11c). The studied serpentinites and ophicalcites are further distinguished by their complementary Sr and Ca anomalies: these elements are depleted in serpentinites and enriched in ophicalcites, reflecting the abundance of carbonates in the ophicalcites (Fig. 10c-11c). The kinetics of serpentinization and carbonation reactions are strongly dependent on temperature, with serpentinization most efficient between 250°-350 °C and carbonation below 200 °C (e.g., Kelemen et al., 2011) but structural and textural evidences suggest that the Urdach serpentinites and ophicalcites are likely contemporaneous. The Urdach peridotite massif is associated with two main tectonic features, a crust-mantle detachment and a cover décollement (Lagabrielle et al., 2019b) that likely acted as efficient fluid pathways for seawater-derived hydrothermal fluids and for alkali rich fluids originating from the Paleozoic continental crust and the Triassic sole. Serpentinite and ophicalcite having the same lherzolite protolith, we propose that the development of the two lithologic domains reflect mainly heterogeneous mixing of fluids from these different sources with a compositional control on reaction paths as shown by recent reactive transport experiments (e.g., Escario et al., 2018; Godard et al., 2013; Peuble et al., 2015; Tutolo et al., 2018). Thus, serpentinization was favored in presence of crust derived Si-bearing fluids (e.g., Tutolo et al., 2018) and carbonation developed in presence of high pH serpentine-derived fluids, locally mixed with seawater-derived fluids (e.g., Beard and Hopkinson, 2000; Ludwig et al., 2006; Schwarzenbach et al., 2021). The development of this complex suite of compositionally controlled reaction paths distinguishes seafloor serpentinization at mid-ocean ridges from that observed in the Urdach peridotites.

5.3. *Serpentinization, partitioning of iron and H_2 production*

Serpentinization leads to the oxidation of the ferrous iron liberated by the dissolution of olivine and pyroxene into magnetite, serpentine and/or brucite (Klein et al., 2009; Marcaillou et al., 2011; Seyfried et al., 2007). In the Montaut, Urdach and Turon peridotite massifs, it follows different pathways depending on temperature and on the renewal and composition of reacting fluids. These different serpentinization pathways control the iron redistribution between hydrous phases and magnetite and therefore the local redox. Two groups of serpentinized peridotites are distinguished: (1) the Montaut serpentinized peridotites and Urdach ophicalcites have abundant magnetite (up to 4%) and low iron content in serpentines (< 5 wt%) and; (2) the Turon peridotites and Urdach serpentinites are characterized by the lack of magnetite and high iron content in serpentines (> 5 wt%).

There is abundant evidence of Fe-bearing serpentine in oceanic serpentinites (e.g., Andreani et al., 2013; Bach et al., 2006), but rare evidence for magnetite-poor samples. To our knowledge, magnetite-poor serpentinized peridotites similar to the WP serpentinized peridotites have been reported only at two sites: the Mariana trench forearc and along the Iberia continental margin (Albers et al., 2021; Klein et al., 2013a). Our understanding of serpentinization during retrograde metamorphism is based mainly on studies of peridotites sampled along (ultra-)slow spreading ridges where olivine serpentinization is triggered at relatively high temperatures (250–350 °C) by the infiltration of seawater-derived fluids during mantle exhumation (e.g., Andreani et al., 2007; Bach et al., 2004). This bias in sampling may have led to underestimating the development of different reaction paths for serpentinization characterizing different geodynamic settings (e.g., Peters et al., 2017). We propose that the heterogeneous distribution of magnetite in the studied peridotites is related to differences in the serpentinization conditions recorded by the WP massifs.

Based on theoretical and experimental studies, the lack of magnetite is primarily interpreted as evidence for low temperatures of serpentinization (Beard et al., 2009; Evans et al., 2009; Frost and Beard, 2007; Klein et al., 2009; Klein et al., 2013a; Seyfried et al., 2007). Different serpentinization temperatures are a likely hypothesis for distinguishing the Turon and the Montaut massifs. The Montaut peridotites record a succession of metasomatic and alteration sequences indicating the continuous presence of fluids, and the onset of serpentinization likely occurred when the temperature conditions became favorable (<450 °C; Bach et al., 2004). In contrast, the lack of magnetite in the serpentinized Turon peridotites is likely related to the lack of brittle faults providing deep fluid pathways, and thus the late penetration of fluids when peridotites had cooled down to temperatures <200 °C. However, the processes controlling the distribution of magnetite in the Urdach massif are probably more complex. The different reaction paths forming the magnetite-poor serpentinite and the magnetite-bearing ophicalcite were not associated with different cooling rates, and elemental transport throughout the peridotite basement was efficient during serpentinization and carbonation. In this context, local changes in fluid-rock compositions suggested by trace element distribution may have impacted also the formation of magnetite (Bach et al., 2006; Frost and Beard, 2007; Klein et al., 2009; Syverson et al., 2017): the stability of magnetite is limited at high silica activity and magnetite-poor serpentinites were likely formed after crust-derived fluids. In contrast, magnetite-bearing ophicalcites result from fluid-rock reactions with high pH and seawater-, and serpentine-derived fluids. Further studies are required to test this scenario and assess its impact on serpentinization-driven H_2

production.

Our results suggest strong linkages between the development of large trans-lithospheric faults and serpentinization: these faults acted as efficient pathways for the infiltration of hydrothermal fluid(s) into the cooling WP peridotites thus controlling the onset of serpentinization. A recent publication (Lefeuvre et al., 2021) shows the occurrence of hydrogen gas seepages along NPFZ, close to the studied massifs, suggesting that serpentinization-driven H_2-production continued during Pyrenean orogeny. The early development of a large-scale fault network during mid-Cretaceous continental extension (e.g. Lagabrielle et al., 2019a) structured the lithospheric mantle creating mechanically weak faults and focused flow zones that remained active over the complex tectonic history of the Pyrenean belt until today. However, serpentinization today likely affects peridotite bodies deeper than the studied peridotite massifs, which display little evidence of late orogenic serpentinization: the latest structural evidences of serpentinization in our samples is the formation of extensive veinlets (Montaut, Urdach) and low temperature alteration consists mostly in pedogenetic weathering and/or the formation of clays (Montaut). The differences in serpentinization pathways from one WP peridotite massif to the other are related mainly to their position along the progressively stretched transition from sub-continental (Montaut, Turon) to seafloor (Urdach) environments during this process, and thus provide first a unique overview of the mechanisms driving serpentinization along magma poor passive margins.

6. Summary and conclusions

We studied the petrology, mineralogy and geochemistry of 32 variably serpentinized peridotites samplese from three Western Pyrenean peridotite massifs, interpreted as sampling segments of a fossil hyper-extended domain. They are mainly fertile peridotites, similar to the refertilized subcontinental lithospheric mantle exposed in the EP peridotite massifs, although the WP peridotites show higher degree of hydrothermal alteration than EP peridotites. The three massifs display contrasted hydrothermal alteration with strong heterogeneities in the abundance and nature of secondary minerals and in the distribution of fluid mobile and highly incompatible elements. We highlighted three types of serpentinization associated with the different structural context of the three massifs:

(1) The Montaut massif records a sequence of hydrothermal alteration with the formation of tremolite, talc and chlorite together with serpentine and magnetite. These mineral assemblages suggest that hydrothermal alteration occurred at temperatures ranging between ~450 °C and 200 °C (Klein et al., 2013a; Rouméjon et al., 2018). It attests of the continuous presence of fluids during cooling probably transported through a major fault system that acted as an extensional detachment before its inversion as the NPFT.
(2) The Turon peridotites comprise mainly mylonites. They record the localization of deformation during mantle extension. They are the least serpentinized of the studied WP peridotites and comprise no magnetite. The lack of magnetite may result from the low degree of serpentinization and/or a serpentinization temperature < 200 °C. Turon shows little evidences of brittle faulting that would have favored the penetration of fluids and we propose that it is the lack of such flow paths that limited serpentinization in this massif.
(3) The Urdach massif records mantle exhumation at the seafloor along two main extensional detachments (later inverted as thrusts) that acted also as main fluid pathways during this process. It comprises magnetite-poor serpentinites and magnetite-rich ophicalcites, the latter being located close to the massif surface. There is no evidence for different cooling history between the serpentinite-dominated and ophicalcite-dominated domains. Furthermore, cross-cutting relationships of serpentine and calcite veins and the peridotite basement support that serpentinization and carbonation reactions were likely contemporaneous suggesting a dominant control of flow and composition of fluids in the development of serpentinite-dominated and ophicalcite-dominated domains at Urdach.

All WP peridotites display selective enrichments in FME compared to EP peridotites as expected from their higher degree of hydrothermal alteration. The compositions of these elements for hydrothermally altered peridotites overlap with that of neighboring dominantly siliclastic sediments suggesting that serpentinizing fluids were mostly derived from, and/or interacted with, crustal lithologies. The differences of reaction paths and geochemistry between oceanic serpentinization and the trends observed in the three studied massifs can be related to the coupling of temperature, fluid infiltration and fluid composition. These parameters vary from one massif to the other, depending of their structural position along the fossil Pyrenean passive margin: the Montaut massifs remained below a few hundred of meters of continental crust and pre-rift sediments and the Turon massif was directly in contact with the pre-rift, while the Urdach massif was directly exposed to the seafloor. This structural configuration directly influences the source of hydrothermal fluids with the most basinward peridotites reflecting mixing with seawater and the most continent-ward peridotites showing sediment-derived fluids.

The development of complex hydrodynamic, temperature and compositional pathways for serpentinization has potential consequences for the evaluation of the redox budget of serpentinization along passive margins when compared to oceanic serpentinites. Iron oxidation and redistribution in secondary minerals control the local redox with direct consequences on H_2 production (Andreani et al., 2013; Klein et al., 2009; Marcaillou et al., 2011) and the formation of H_2 seepages, springs and hydrothermal vents (e.g., Fruh-Green et al., 2003; Gaucher, 2020; Lefeuvre et al., 2021). A better understanding of these mechanisms is required to estimate their potential for H_2 production and assess possible differences between geodynamic environments.

Declaration of Competing Interest

The authors declare that they have no known competing financial interests or personal relationships that could have appeared to influence the work reported in this paper.

Acknowledgments

We thank Guillaume Barré for his assistance and discussions during field work. We thank C. Nevado and D. Delmas for thin section preparation and F. Barou and R. Lafay for their help during EBSD and EPMA analyses at Géosciences Montpellier. We thank also O. Bruguier and T. Michel for their support for LA-ICPMS (AETE-ISO, OSU OREME, U. Montpellier) and RAMAN (Laboratoire Charles Coulomb, U. Montpellier) analyses respectively and J.-L. Devidal for the complementary LA-ICPMS measurements realized at the Laboratoire Magmas et Volcans facility (U. Clermont Auvergne, France) during the COVID-19 crisis. We would also like to thank G. Shellnutt for editorial handling and two anonymous reviewers for their comments and suggestions on the manuscript.

This work was supported by TOTAL E&P Recherche Developpement (grant number TOTAL FR00009409/U. Montpellier 170371/ CNRS 162592).

Appendix A. Supplementary data

Supplementary data to this article can be found online at https://doi.org/10.1016/j.lithos.2021.106521.

References

Albers, E., Bach, W., Pérez-Gussinyé, M., McCammon, C., Frederichs, T., 2021. Serpentinization-driven H2 production from continental break-up to mid-ocean ridge spreading: unexpected high rates at the west iberia margin. Front. Earth Sci. 9.

Andreani, M., Baronnet, A., Boullier, A.M., Gratier, J.P., 2004. A microstructural study of a "crack-seal" type serpentine vein using SEM and TEM techniques. Eur. J. Mineral. 16, 585–595.

Andreani, M., Mével, C., Boullier, A.M., Escartín, J., 2007. Dynamic control on serpentine crystallization in veins: constraints on hydration processes in oceanic peridotites. Geochem. Geophys. Geosyst. 8 n/a-n/a.

Andreani, M., Muñoz, M., Marcaillou, C., Delacour, A., 2013. μXANES study of iron redox state in serpentine during oceanic serpentinization. Lithos 178, 70–83.

Bach, W., Garrido, C.J., Paulick, H., Harvey, J., Rosner, M., 2004. Seawater-peridotite interactions: First insights from ODP Leg 209, MAR 15°N. Geochem. Geophys. Geosyst. 5 n/a-n/a.

Bach, W., Paulick, H., Garrido, C.J., Ildefonse, B., Meurer, W.P., Humphris, S.E., 2006. Unraveling the sequence of serpentinization reactions: petrography, mineral chemistry, and petrophysics of serpentinites from MAR 15°N (ODP Leg 209, Site 1274). Geophys. Res. Lett. 33.

Beard, J.S., Hopkinson, L., 2000. A fossil, serpentinization-related hydrothermal vent, Ocean Drilling Program Leg 173, Site 1068 (Iberia Abyssal Plain): some aspects of mineral and fluid chemistry. J. Geophys. Res. Solid Earth 105, 16527–16539.

Beard, J.S., Frost, B.R., Fryer, P., McCaig, A., Searle, R., Ildefonse, B., Zinin, P., Sharma, S.K., 2009. Onset and Progression of Serpentinization and Magnetite Formation in Olivine-rich Troctolite from IODP Hole U1309D. J. Petrol. 50, 387–403.

Bodinier, J.L., Godard, M., 2013. Orogenic, Ophiolitic, and Abyssal Peridotites. Treatise on geochemistry.

Bodinier, J.L., Dupuy, C., Dostal, J., 1988. Geochemistry and petrogenesis of Eastern Pyrenean peridotites. Geochim. Cosmochim. Acta 52, 2893–2907.

Bodinier, J.L., Vasseur, G., Vernieres, J., Dupuy, C., Fabries, J., 1990. Mechanisms of Mantle metasomatism: geochemical evidence from the Lherz Orogenic Peridotite. J. Petrol. 31, 597–628.

Boillot, G., Beslier, M.O.C., 1992. Seismic image of undercrusted serpentinite beneath a rifted margin. Terra Nova 4, 25–33.

Brey, G.P., Köhler, T., 1990. Geothermobarometry in four-phase lherzolites II. New thermobarometers, and practical assessment of existing thermobarometers. J. Petrol. 31, 1353–1378.

Clerc, C., Lagabrielle, Y., 2014. Thermal control on the modes of crustal thinning leading to mantle exhumation: insights from the Cretaceous Pyrenean hot paleomargins. Tectonics 33, 1340–1359.

Clerc, C., Lagabrielle, Y., Neumaier, M., Reynaud, J.Y., de Saint Blanquat, M., 2012. Exhumation of subcontinental mantle rocks: evidence from ultramafic-bearing clastic deposits nearby the Lherz peridotite body, French Pyrenees. Bulletin de la Société géologique de France 183, 443–459.

Clerc, C., Boulvais, P., Lagabrielle, Y., de Saint Blanquat, M., 2013. Ophicalcites from the northern Pyrenean belt: a field, petrographic and stable isotope study. Int. J. Earth Sci. 103, 141–163.

Clerc, C., Lahfid, A., Monié, P., Lagabrielle, Y., Chopin, C., Poujol, M., Boulvais, P., Ringenbach, J.C., Masini, E., de St Blanquat, M., 2015. High-temperature metamorphism during extreme thinning of the continental crust: a reappraisal of the North Pyrenean passive paleomargin. Solid Earth 6, 643–668.

Corre, B., Boulvais, P., Boiron, M.C., Lagabrielle, Y., Marasi, L., Clerc, C., 2018. Fluid circulations in response to mantle exhumation at the passive margin setting in the north Pyrenean zone, France. Mineral. Petrol. 112, 647–670.

DeFelipe, I., Pedreira, D., Pulgar, J.A., Iriarte, E., Mendia, M., 2017. Mantle exhumation and metamorphism in the Basque-Cantabrian Basin (NSpain): Stable and clumped isotope analysis in carbonates and comparison with ophicalcites in the North-Pyrenean Zone (Urdach and Lherz). Geochem. Geophys. Geosyst. 18, 631–652.

Deschamps, F., Godard, M., Guillot, S., Chauvel, C., Andreani, M., Hattori, K., Wunder, B., France, L., 2012. Behavior of fluid-mobile elements in serpentines from abyssal to subduction environments: examples from Cuba and Dominican Republic. Chem. Geol. 312-313, 93–117.

Deschamps, F., Godard, M., Guillot, S., Hattori, K., 2013. Geochemistry of subduction zone serpentinites: a review. Lithos 178, 96–127.

Doebelin, N., Kleeberg, R., 2015. Profex: a graphical user interface for the Rietveld refinement program BGMN. J. Appl. Crystallogr. 48, 1573–1580.

Downes, H., Bodinier, J.-L., Thirlwall, M.F., Lorand, J.-P., 1991. REE and Sr-Nd isotopic geochemistry of eastern pyrenean peridotite massifs: sub-continental lithospheric mantle modified by continental magmatism. J. Petrol. 2, 97–115.

Escario, S., Godard, M., Gouze, P., Leprovost, R., 2018. Experimental study of the effects of solute transport on reaction paths during incipient serpentinization. Lithos 323, 191–207.

Escartín, J., Mével, C., MacLeod, C.J., McCaig, A.M., 2003. Constraints on deformation conditions and the origin of oceanic detachments: the Mid-Atlantic Ridge core complex at 15°45′N. Geochem. Geophys. Geosyst. 4.

Evans, B.W., 2008. Control of the products of serpentinization by the Fe2+Mg-1 Exchange potential of olivine and orthopyroxene. J. Petrol. 49, 1873–1887.

Evans, B.W., Kuehner, S.M., Chopelas, A., 2009. Magnetite-free, yellow lizardite serpentinization of olivine websterite, Canyon Mountain complex, NE Oregon. Am. Mineral. 94, 1731–1734.

Evans, B.W., Hattori, K., Baronnet, A., 2013. Serpentinite: what, why, where? Elements 9, 99–106.

Fabriès, J., Lorand, J.P., Bodinier, J.L., 1998. Petrogenetic evolution of orogenic lherzolite massifs in the central and western Pyrenees. Tectonophysics 292, 145–167.

Fabriès, J., Lorand, J.P., Bodinier, J.L., Dupuy, C., 1991. Evolution of the Upper Mantle beneath the Pyrenees: evidence from Orogenic Spinel Lherzolite Massifs. J. Petrol. 2, 55–76.

Frost, B.R., 1985. On the stability of sulfides, oxides, and native metals in serpentinite. J. Petrol. 26, 31–63.

Frost, B.R., Beard, J.S., 2007. On silica activity and serpentinization. J. Petrol. 48, 1351–1368.

Fruh-Green, G.L., Kelley, D.S., Bernasconi, S.M., Karson, J.A., Ludwig, K.A., Butterfield, D.A., Boschi, C., Proskurowski, G., 2003. 30,000 years of hydrothermal activity at the lost city vent field. Science 301, 495–498.

Fumagalli, P., Borghini, G., Rampone, E., Poli, S., 2017. Experimental calibration of Forsterite–Anorthite–Ca-Tschermak–Enstatite (FACE) geobarometer for mantle peridotites. Contrib. Mineral. Petrol. 172, 38.

Gaucher, E.C., 2020. New Perspectives in the Industrial Exploration for Native Hydrogen. Elements 16, 8–9.

Godard, M., Luquot, L., Andreani, M., Gouze, P., 2013. Incipient hydration of mantle lithosphere at ridges: a reactive-percolation experiment. Earth Planet. Sci. Lett. 371-372, 92–102.

Gueddari, K., Piboule, M., Amossé, J., 1996. Differentiation of platinum-group elements (PGE) and of gold during partial melting of peridotites in the lherzolitic massifs of the Betico-Rifean range (Ronda and Beni Bousera). Chem. Geol. 134, 181–197.

Guillot, S., Schwartz, S., Reynard, B., Agard, P., Prigent, C., 2015. Tectonic significance of serpentinites. Tectonophysics 646, 1–19.

Hart, S.R., Zindler, A., 1986. In search of a bulk-Earth composition. Chem. Geol. 57, 247–267.

Hébert, R., Gueddari, K., Lafleche, M.R., Beslier, M.O., Gardien, V., 2001. Petrology and geochemistry of exhumed peridotites and gabbros at non-volcanic margins: ODP Leg 173 West Iberia ocena-continent transition zone. Geol. Soc. Lond., Spec. Publ. 187, 161–189.

Jagoutz, E., Palme, H., Baddenhausen, H., Blum, K., Cendales, M., Dreibus, G., Spettel, B., Lorenz, V., Wänke, H., 1979. He abundances of major, minor and trace elements in the earth's mantle as derived from primitive ultramafic nodules. In: Lunar and Planetary Science Conference Proceedings, 10, pp. 2031–2050.

Kelemen, P.B., Matter, J., Streit, E.E., Rudge, J.F., Curry, W.B., Blusztajn, J., 2011. Rates and mechanisms of mineral carbonation in peridotite: natural processes and recipes for enhanced, in situ CO2 capture and storage. Annu. Rev. Earth Planet. Sci. 39, 545–576.

Klein, F., Bach, W., Humphris, S.E., Kahl, W.A., Jons, N., Moskowitz, B., Berquo, T.S., 2013a. Magnetite in seafloor serpentinite–some like it hot. Geology 42, 135–138.

Klein, F., Bach, W., Jöns, N., McCollom, T., Moskowitz, B., Berquó, T., 2009. Iron partitioning and hydrogen generation during serpentinization of abyssal peridotites from 15°N on the Mid-Atlantic Ridge. Geochim. Cosmochim. Acta 73, 6868–6893.

Klein, F., Bach, W., McCollom, T.M., 2013b. Compositional controls on hydrogen generation during serpentinization of ultramafic rocks. Lithos 178, 55–69.

Klein, F., Humphris, S.E., Guo, W., Schubotz, F., Schwarzenbach, E.M., Orsi, W.D., 2015. Fluid mixing and the deep biosphere of a fossil Lost City-type hydrothermal system at the Iberia Margin. Proc. Natl. Acad. Sci. U. S. A. 112, 12036–12041.

Kodolányi, J., Pettke, T., Spandler, C., Kamber, B.S., Gméling, K., 2012. Geochemistry of ocean floor and fore-arc serpentinites: constraints on the ultramafic input to subduction zones. J. Petrol. 53, 235–270.

Labaume, P., Teixell, A., 2020. Evolution of salt structures of the Pyrenean rift (Chaînons Béarnais, France): from hyper-extension to tectonic inversion. Tectonophysics 785.

Lafuente, B., Downs, R.T., Yang, H., Stone, N., 2015. The power of databases: The RRUFF project. Highlights in Mineralogical Crystallography.

Lagabrielle, Y., Asti, R., Fourcade, S., Corre, B., Labaume, P., Uzel, J., Clerc, C., Lafay, R., Picazo, S., 2019a. Mantle exhumation at magma-poor passive continental margins. Part II: Tectonic and metasomatic evolution of large-displacement detachment faults preserved in a fossil distal margin domain (Saraillé lherzolites, northwestern Pyrenees, France). BSGF - Earth Sci. Bull. 190.

Lagabrielle, Y., Asti, R., Fourcade, S., Corre, B., Poujol, M., Uzel, J., Labaume, P., Clerc, C., Lafay, R., Picazo, S., Maury, R., 2019b. Mantle exhumation at magma-poor passive continental margins. PartI. 3Darchitecture and metasomatic evolution of a fossil exhumed mantle domain (Urdach lherzolite, North-Western Pyrenees, France). BSGF - Earth Sci. Bull. 190.

Lagabrielle, Y., Bodinier, J.-L., 2008. Submarine reworking of exhumed subcontinental mantle rocks: field evidence from the Lherz peridotites, French Pyrenees. Terra Nova 20, 11–21.

Lagabrielle, Y., Labaume, P., de Saint Blanquat, M., 2010. Mantle exhumation, crustal denudation, and gravity tectonics during Cretaceous rifting in the Pyrenean realm (SW Europe): Insights from the geological setting of the lherzolite bodies. Tectonics 29 n/a-n/a.

Lefeuvre, N., Truche, L., Donze, F.V., Ducoux, M., Barré, G., Fakoury, R.-A., Calassou, S., Gaucher, E., 2021. Native H2 exploration in the Western Pyrenean Foothills. Geochem. Geophys. Geosyst. 22.

Le Roux, V., Bodinier, J.L., Tommasi, A., Alard, O., Dautria, J.M., Vauchez, A., Riches, A. J.V., 2007. The Lherz spinel lherzolite: refertilized rather than pristine mantle. Earth Planet. Sci. Lett. 259, 599–612.

Liang, Y., Sun, C., Yao, L., 2013. A REE-in-two-pyroxene thermometer for mafic and ultramafic rocks. Geochim. Cosmochim. Acta 102, 246–260.

Ludwig, K.A., Kelley, D.S., Butterfield, D.A., Nelson, B.K., Früh-Green, G., 2006. Formation and evolution of carbonate chimneys at the lost City Hydrothermal Field. Geochim. Cosmochim. Acta 70, 3625–3645.

Malvoisin, B., Brunet, F., Carlut, J., Rouméjon, S., Cannat, M., 2012. Serpentinization of oceanic peridotites: 2. Kinetics and processes of San Carlos olivine hydrothermal alteration. J. Geophys. Res. Solid Earth 117 n/a-n/a.
Manatschal, G., 2004. New models for evolution of magma-poor rifted margins based on a review of data and concepts from West Iberia and the Alps. Int. J. Earth Sci. 93.
Manatschal, G., Engström, A., Desmurs, L., Schaltegger, U., Cosca, M., Müntener, O., Bernoulli, D., 2006. What is the tectono-metamorphic evolution of continental break-up: the example of the Tasna Ocean–Continent Transition. J. Struct. Geol. 28, 1849–1869.
Marcaillou, C., Muñoz, M., Vidal, O., Parra, T., Harfouche, M., 2011. Mineralogical evidence for H2 degassing during serpentinization at 300°C/300bar. Earth Planet. Sci. Lett. 303, 281–290.
McCarthy, A., Tugend, J., Mohn, G., Candioti, L., Chelle-Michou, C., Arculus, R., Schmalholz, S.M., Müntener, O., 2020. A case of Ampferer-type subduction and consequences for the Alps and the Pyrenees. Am. J. Sci. 320, 313–372.
McDonough, W.F., Sun, S.S., 1995. The composition of the Earth. Chem. Geol. 120, 223–253.
Mével, C., 2003. Serpentinization of abyssal peridotites at mid-ocean ridges. Compt. Rendus Geosci. 335, 825–852.
Muñoz, M., Pascarelli, S., Aquilanti, G., Narygina, O., Kurnosov, A., Dubrovinsky, L., 2008. Hyperspectral micro–XANES mapping in the diamond–anvil cell: Analytical procedure applied to the decomposition of (Mg,Fe)–ringwoodite at the upper/lower mantle boundary. High Pressure Research 28, 665–673.
Muntener, O., Manatschal, G., Desmurs, L., Pettke, T., 2009. Plagioclase peridotites in ocean-continent transitions: refertilized mantle domains generated by melt stagnation in the shallow mantle lithosphere. J. Petrol. 51, 255–294.
Paulick, H., Bach, W., Godard, M., De Hoog, J.C.M., Suhr, G., Harvey, J., 2006. Geochemistry of abyssal peridotites (Mid-Atlantic Ridge, 15°20′N, ODP Leg 209): implications for fluid/rock interaction in slow spreading environments. Chem. Geol. 234, 179–210.
Pérez-Gussinyé, M., Reston, T.J., 2001. Rheological evolution during extension at nonvolcanic rifted margins: Onset of serpentinization and development of detachments leading to continental breakup. J. Geophys. Res. Solid Earth 106, 3961–3975.
Peters, D., Bretscher, A., John, T., Scambelluri, M., Pettke, T., 2017. Fluid-mobile elements in serpentinites: Constraints on serpentinisation environments and element cycling in subduction zones. Chem. Geol. 466, 654–666.
Peuble, S., Godard, M., Luquot, L., Andreani, M., Martinez, I., Gouze, P., 2015. CO2 geological storage in olivine rich basaltic aquifers: New insights from reactive-percolation experiments. Appl. Geochem. 52, 174–190.
Plümper, O., Røyne, A., Magrasó, A., Jamtveit, B., 2012. The interface-scale mechanism of reaction-induced fracturing during serpentinization. Geology 40, 1103–1106.
Rouméjon, S., Früh-Green, G.L., Orcutt, B.N., 2018. Alteration heterogeneities in peridotites exhumed on the southern wall of the Atlantis Massif (IODP expedition 357). J. Petrol. 59, 1329–1358.
Salters, V.J., Stracke, A., 2004. Composition of the depleted mantle. Geochem. Geophys. Geosyst. 5, 5.
Schwarzenbach, E.M., Früh-Green, G.L., Bernasconi, S.M., Alt, J.C., Plas, A., 2013. Serpentinization and carbon sequestration: a study of two ancient peridotite-hosted hydrothermal systems. Chem. Geol. 351, 115–133.
Schwarzenbach, E.M., Vogel, M., Früh-Green, G.L., Boschi, C., 2021. Serpentinization, Carbonation, and Metasomatism of Ultramafic Sequences in the Northern Apennine Ophiolite (NW Italy). J. Geophys. Res. Solid Earth 126.
Seyfried, W.E., Foustoukos, D.I., Fu, Q., 2007. Redox evolution and mass transfer during serpentinization: an experimental and theoretical study at 200°C, 500bar with implications for ultramafic-hosted hydrothermal systems at Mid-Ocean Ridges. Geochim. Cosmochim. Acta 71, 3872–3886.
Syverson, D.D., Tutolo, B.M., Borrok, D.M., Seyfried, W.E., 2017. Serpentinization of olivine at 300 °C and 500 bars: an experimental study examining the role of silica on the reaction path and oxidation state of iron. Chem. Geol. 475, 122–134.
Teixell, A., Labaume, P., Ayarza, P., Espurt, N., de Saint Blanquat, M., Lagabrielle, Y., 2018. Crustal structure and evolution of the Pyrenean-Cantabrian belt: a review and new interpretations from recent concepts and data. Tectonophysics 724-725, 146–170.
Tutolo, B.M., Luhmann, A.J., Tosca, N.J., Seyfried, W.E., 2018. Serpentinization as a reactive transport process: the brucite silicification reaction. Earth Planet. Sci. Lett. 484, 385–395.
Van Acken, D., Becker, H., Walker, R.J., 2008. Refertilization of Jurassic oceanic peridotites from the Tethys Ocean—implications for the Re–Os systematics of the upper mantle. Earth Planet. Sci. Lett. 268, 171–181.
Van der Wal, D., Bodinier, J.L., 1996. Origin of the recrystallisation front in the Ronda peridotite by km-scale pervasive porous melt flow. Contrib. Mineral. Petrol. 122, 387–405.
Vissers, R.L.M., Drury, M.R., Newman, J., Fliervoet, T.F., 1997. Mylonitic deformation in upper mantle peridotites of the North Pyrenean Zone (France): implications for strength and strain localization in the lithosphere. Tectonophysics 279, 303–325.
Wells, P.R., 1977. Pyroxene thermometry in simple and complex systems. Contrib. Mineral. Petrol. 62, 129–139.